Astronomy & Astrophysics manuscript no. paper
July 30, 2012

© ESO 2012

arXiv:1207.6410v1 [astro-ph.CO] 26 Jul 2012

On the Physics of Radio Halos in Galaxy Clusters: Scaling Relations and Luminosity Functions

Fabio Zandanel[1*], Christoph Pfrommer[2†], and Francisco Prada[3,4,1§]

[1] Instituto de Astrofísica de Andalucía (CSIC), Glorieta de la Astronomía, E-18080 Granada, Spain
[2] Heidelberg Institute for Theoretical Studies, Schloss-Wolfsbrunnenweg 35, D-69118 Heidelberg, Germany
[3] Campus of International Excellence UAM+CSIC, Cantoblanco, E-28049 Madrid, Spain
[4] Instituto de Física Teórica, (UAM/CSIC), Universidad Autónoma de Madrid, Cantoblanco, E-28049 Madrid, Spain

Received XXX / Accepted XXX

ABSTRACT

The underlying physics of giant radio halos and mini halos in galaxy clusters is still an open question, which becomes more pressing with the growing number of detections. In this paper, we explore the possibility that radio-emitting electrons are generated in hadronic cosmic ray (CR) proton interactions with ambient thermal protons of the intra-cluster medium. Our CR model derives from cosmological hydrodynamical simulations of cluster formation and additionally accounts for CR transport in the form of CR streaming and diffusion. This opens the possibility of changing the radio halo luminosity by more than an order of magnitude on a dynamical time scale. We build a mock galaxy cluster catalog from the large MultiDark N-body ΛCDM simulation by adopting a phenomenological gas density model for each cluster based on X-ray measurements that matches Sunyaev-Zel'dovich and X-ray scaling relations and luminosity function. Using magnetic field strength estimates from Faraday rotation measure studies, our model successfully reproduces the observed surface brightness profiles of giant radio halos (Coma, A2163) as well as radio mini-halos (Perseus, Ophiuchus), while obeying upper limits on the gamma-ray emission in these clusters. Because of CR streaming transport and the different scalings of the X-ray luminosity, L_X, and the Sunyaev-Zel'dovich flux, Y, with respect to gas density, our model is also able to simultaneously reproduce the observed bimodality of radio-loud and radio-quiet clusters at the same L_X as well as the unimodal distribution of radio-halo luminosity versus Y; thereby suggesting a physical solution to this apparent contradiction. For a plausible fraction of 10% radio-loud clusters, our model matches the NVSS radio-halo luminosity function. Constructing an analytical radio-halo luminosity function, we demonstrate the unique prospects for low-frequency radio surveys (such as the LOFAR Tier 1 survey) to detect $\sim$ 3500 radio halos back to redshift two and to probe the underlying physics of radio halos. We will make our cosmologically complete multi-frequency mock catalogs for the (non-)thermal cluster emission at different redshifts publicly and freely available on-line through the MultiDark database.

Key words. Cosmology: theory - Cosmology: diffuse radiation - Galaxies: clusters: intracluster medium - Radio continuum: galaxies - Gamma rays: galaxies: clusters - Astroparticle physics

1. Introduction

The presence of large-scale diffuse radio synchrotron emission in clusters of galaxies proves the existence of relativistic electrons and magnetic fields permeating the intra-cluster medium (ICM) (see, e.g, Feretti et al. 2004). Diffuse cluster radio emission can be separated in two classes: radio halos and radio relics (see, e.g., Kempner et al. 2004; Ferrari et al. 2008). Radio (mini-)halos (RHs) are centered on clusters and characterized by a regular and unpolarized morphology, resembling the morphology of the thermal X-ray emission. On the contrary, radio relics typically lie at the cluster outskirts, have an irregular morphology, and often show a high degree of polarization. While relics seem to directly trace structure formation shocks (see, e.g., van Weeren et al. 2010), the explanation for the RH phenomenon is challenging and still an open question.

Two principal models have been proposed to explain RHs. In the "hadronic model" the radio emitting electrons are produced in hadronic cosmic ray (CR) proton interactions with protons of the ambient thermal ICM, requiring only a very modest fraction of (at most) a few percent of CR-to-thermal pressure (see Dennison 1980; Vestrand 1982; Blasi & Colafrancesco 1999; Dolag & Enßlin 2000; Miniati et al. 2001b,a; Pfrommer & Enßlin 2003, 2004a,b; Blasi et al. 2007; Pfrommer et al. 2008; Pfrommer 2008; Kushnir et al. 2009; Donnert et al. 2010a,b; Keshet & Loeb 2010; Keshet 2010; Enßlin et al. 2011). CR protons and heavier nuclei, like electrons, can be accelerated and injected into the ICM by structure formation shocks, active galactic nuclei (AGN) and galactic winds. Due to their higher masses with respect to electrons, CR protons are accelerated more efficiently to relativistic energies and are expected to show a ratio of the spectral energy flux of CR protons to electrons above 1 GeV of about 100, similarly to what is observed in our Galaxy (Schlickeiser 2002). Additionally, CR protons have a radiative cooling time larger than that of the electrons by the square of the mass ratio and therefore can accumulate in clusters for cosmological times (Völk et al. 1996). Indeed, CR electrons suffer more severe energy losses via synchrotron and inverse Compton emission at particle energies $E \gtrsim 100$ MeV, and Coulomb losses below that energy range.

In the "re-acceleration model", RHs are thought to be the result of re-acceleration of electrons through interactions

---

* fabio@iaa.es
† christoph.pfrommer@h-its.org
§ fprada@iaa.es

with plasma waves during powerful states of ICM turbulence, as a consequence of a cluster merger (see Schlickeiser et al. 1987; Giovannini et al. 1993; Gitti et al. 2002; Brunetti et al. 2004; Brunetti & Blasi 2005; Brunetti & Lazarian 2007, 2011; Brunetti et al. 2009). This, however, requires a sufficiently long-lived CR electron population at energies around 100 MeV which has to be continuously maintained by re-acceleration at a rate faster than the cooling processes. We refer the reader to Enßlin et al. (2011) for a discussion on the strengths and weaknesses of these two models.

RHs can be divided in two classes. Giant radio halos are typically associated with merging clusters and have large extensions, e.g., the Coma radio halo has an extension of about 2 Mpc. Radio mini-halos are associated with relaxed clusters that harbor a cool core and typically extend over a few hundred kilo-parsecs, e.g., the Perseus radio mini-halo has an extension of about 0.2 Mpc. The observed morphological similarities with the thermal X-ray emission suggests that RHs may be of hadronic origin. In fact, cool-core clusters (CCCs) are characterized by high thermal X-ray emissivities and ICM densities that are more peaked in comparison to (merging) non cool-core clusters (NCCCs) (see, e.g., Croston et al. 2008). This distinct difference in the ICM density structure of CCCs and NCCCs is reflected in the morphology of the two observed classes of RHs.

The RH luminosity seems to be correlated to the thermal X-ray luminosity (see, e.g., Brunetti et al. 2009; Enßlin et al. 2011). However, a large fraction of clusters does not exhibit significant diffuse synchrotron emission. Galaxy clusters with the same thermal X-ray luminosity show an apparent bimodality with respect to their radio luminosity. Either they harbor a RH or they do not have any detectable diffuse radio emission (Brunetti et al. 2009; Enßlin et al. 2011). This suggests the existence of a switch-on/switch-off mechanism that is able to change the radio luminosity by more than one order of magnitude. While such a mechanism could be easily realized in the framework of the re-acceleration model (Brunetti et al. 2009), the *classical* hadronic model predicts the presence of RHs in all clusters. The failure to reproduce the observed cluster radio-to-X-ray bimodality was one of the main criticisms against the hadronic model. Additionally, the *classical* hadronic model cannot reproduce some spectral features observed in clusters, such as the total spectral curvature claimed in the Coma radio halo or the spectral steepening observed at the boundary of some RHs. However, the recent report of spectral flattening with energy of the radio halo in A2256 (van Weeren et al. 2012) rises the question whether such a variability among different source of the same class is inherent to the underlying physics or whether it is a signature of uncertainty in the algorithms used to process the data.

In a recent work, Enßlin et al. (2011) assess these problems of the *classical* hadronic model by analyzing CR transport processes within a cluster. While CR advection with turbulently driven flows results in centrally enhanced CR profiles, the propagation in form of CR streaming and diffusion produces a flattening of CR profiles. Hence, different CR transport phenomena may also account for the observed bimodality of the radio luminosity in the hadronic model and may also explain the spectral features observed in some clusters (Enßlin et al. 2011). Note that these CR transport phenomena were not considered in earlier analytical works (see, e.g., Pfrommer & Enßlin 2004a) as well as in previous hydrodynamic simulations (see, e.g., Miniati et al. 2001a; Pfrommer et al. 2008; Pinzke & Pfrommer 2010).

More recently, Basu (2012) presented the first scaling relations between RH luminosity and Sunyaev-Zel'dovich (SZ) flux measurements, using the *Planck* cluster catalogue. While the correlation agrees with previous scaling measurements based on X-ray data, there is no indication for a bimodal cluster population dividing clusters into radio-loud and radio-quiet objects at fixed SZ flux. While the SZ flux correlates tightly with cluster mass, the X-ray luminosity, L_{X}, exhibits a larger scatter. The CCCs predominantly populate the high-L_{X} tail (at any cluster temperature) and make up approximately half of the radio-quiet objects (Enßlin et al. 2011). This suggests that the switch-on/switch-off mechanism may not operate at fixed L_{X} but also causes an evolution of that quantity. As the cluster relaxes after a merger, it cools and forms a denser core. Simultaneously, L_{X} is expected to *increase* which may simultaneously *decrease* the radio luminosity owing to the decaying turbulence that is responsible in maintaining the radio emission in either model (that accounts for microscopic CR transport).

An observational test that is able to disentangle between the hadronic and re-acceleration models is the gamma-ray emission resulting from neutral pion decays, a secondary product of the hadronic CR interaction with protons of the ICM, which is not predicted by the re-acceleration model. Such observational efforts have been undertaken in the last few years (for space-based cluster observations in the GeV-band, see Reimer et al. 2003; Ackermann et al. 2010a,b; Zimmer et al. 2012; Han et al. 2012; for ground-based observations in the energy band $\gtrsim$ 100 GeV, see Perkins et al. 2006; Perkins 2008; Aharonian et al. 2009a,b; Domainko et al. 2009; Galante et al. 2009; Kiuchi et al. 2009; Acciari et al. 2009; Aleksić et al. 2010, 2012) without being able to detect cluster gamma-ray emission[1]. Gamma-ray limits enable us to put significant constraints on the relative CR pressure contributions. The long observational campaign of the Perseus galaxy cluster performed by the Major Atmospheric Gamma-ray Cherenkov (MAGIC) telescopes constrains the cluster average CR-to-thermal pressure to be less than a few percent (Aleksić et al. 2010, 2012). Comparing the corresponding upper limits to predictions of simulations by Pinzke & Pfrommer (2010) constrains the maximum CR acceleration efficiency at structure formation shocks to be $<$ 50%. Alternatively, this may indeed suggest the presence of non-negligible CR transport processes into the outer cluster regions as suggested by Enßlin et al. (2011). Constraints at the same level are confirmed by the *Fermi*-Large Area Telescope (LAT) data on the Coma cluster (Pinzke et al. 2011; Zimmer et al. 2012; Han et al. 2012). To summarize, gamma-ray observations are not yet sensitive enough to severely challenge hadronic models of RHs.

An important step towards understanding the generating mechanism of RHs could come from detailed RH population analyses. To date, we know of 53 clusters that harbor RHs (see Feretti et al. 2012, for an almost up-to-date list). Only two X-ray flux-limited studies have been conducted that assess the important question of the RH frequency in clusters (Giovannini et al. 1999; Venturi et al. 2008). Since the number of RHs in such X-ray flux-limited samples is small with typically a few RHs, the conclusions on the underlying physical mechanisms of RHs are not very robust. Fortunately, this is going to change thanks to the next-generation of low-frequency radio observatories such as the Low Frequency Array (LOFAR) which officially started operations in 2010.[2] In fact, a deep cluster survey is part of the LOFAR science key projects and expected to provide a large number of radio-emitting galaxy clusters up to redshift $z \approx 1$ (see, e.g., Cassano et al. 2010; Röttgering et al. 2012). This will hopefully permit to clearly determine the RH phenomenology with respect to galaxy cluster properties such as the fractions of radio-loud/quiet, non cool-core/cool-core, and non-merging/merging clusters, and to explore the role of different parameters like the magnetic field, the CR acceleration efficiency, and CR transport properties.

---

[1] Recently, Han et al. (2012) claimed an evidence for diffuse gamma-ray emission in the *Fermi* satellite data of the Virgo cluster which however needs to be carefully scrutinized by varying the uncertain foreground modeling (for a preliminary assessment of the *Fermi* collaboration, see Elliot Bloom's talk at the UCLA Dark Matter 2012 conference, https://hepconf.physics.ucla.edu/dm12/).

In this work, we use a sample of galaxy clusters up to $z = 1$, obtained from the MultiDark N-body cosmological simulation (Prada et al. 2012). We construct a *phenomenological* model to assign a gas density profile to each halo in the MultiDark simulation that is based on observed X-ray cluster properties. We assume that the RHs are generated by secondaries of hadronic CR interactions with the ICM. In adopting the hadronic scenario, we construct a *hybrid* CR model and merge the result of hydrodynamic simulations by Pinzke & Pfrommer (2010) and the analytical model by Enßlin et al. (2011). As anticipated above, the inclusion of the latter is particularly important as CR transport processes have a dramatic impact on the emission profile and normalization. We will show that this approach enables us not only to reproduce the radio surface brightness profiles but also the radio-to-X-ray and radio-to-SZ scaling relations. Hence, this explicitly demonstrates that the hadronic model is an attractive model that matches all current observational constraints and predicts the luminosity function for the LOFAR cluster survey.

In Section 2, we explain the methodology of assigning gas density profiles to dark matter (DM) halos and demonstrate that the model reproduces the observed SZ and X-ray scaling relations and luminosity function. We then construct the model for the CR distribution in clusters. In Section 3, we apply our model to observed surface brightness profiles of individual RHs and explore the allowable parameter space for CRs and magnetic fields. In Section 4, we compare the modeled radio-to-X-ray and radio-to-SZ scaling relations to current observations and show how they vary for different choices of our CR and magnetic parametrizations. In Section 5, we show the radio luminosity functions, compare them to current observational constraints and provide predictions for the LOFAR cluster survey. Finally, in Section 6, we present our conclusions. In this work, the cluster mass M_Δ and radius R_Δ are defined with respect to a density that is $\Delta = 200$ or $\Delta = 500$ times the *critical* density of the Universe. We adopt density parameters of $\Omega_\mathrm{m} = 0.3$, $\Omega_\Lambda = 0.7$ and today's Hubble constant of $H_0 = 100 \times h_{70}$ km s^{-1} Mpc^{-1} where $h_{70} = 0.7$.

2. Methodology

The two basic ingredients of this work are an N-body, *DM-only* cosmological simulation that we use in constructing our complete cluster sample, and the (non-)thermal emission model. Here, we use the MultiDark simulation that will be described in Section 2.1, along with our final cluster sample. As we will see, for any given cluster, the necessary ingredients for the emission model are mass, temperature, and gas density distribution. We assign to each cluster in that simulation a gas density profile that is phenomenologically constructed from state-of-art X-ray observations, as will be shown in Section 2.2. We will show that this approach can successfully reproduce the known X-ray cluster characteristics, such as the X-ray luminosity function (XLF), the luminosity-mass relation, $L_\mathrm{X} - M$, and the $Y_\mathrm{X} - M$ relation, where $Y_\mathrm{X} = M_\mathrm{gas} k_\mathrm{B} T$ with an X-ray-derived gas mass M_gas and temperature T (Kravtsov et al. 2006). Moreover, we compare our $Y_\mathrm{SZ} - M$ relation with SZ-derived measurements. Only if our model matches available cluster data on the gas properties, we can start to explore different parametrizations of CR physics and its implications for the radio and gamma-ray emission, as will be explained in Section 2.5.

Table 1. Number of halos in the final cluster sample

redshift z	number of halos
0.0	13763
0.2	12398
0.3	10783
0.4	7789
0.61	5187
0.78	3372
1.0	1803

Note. We show the number of halos in our MultiDark snapshots at redshift z for $M_{200} \geq 1 \times 10^{14}\ h^{-1}\ \mathrm{M}_\odot \approx 1.4 \times 10^{14}\ h_{70}^{-1}\ \mathrm{M}_\odot$.

2.1. MultiDark simulation and final cluster sample

The MultiDark simulation used in this work is described in detail in Prada et al. (2012). It is an N-body cosmological simulation done with the Adaptive-Refinement-Tree (ART) code (Kravtsov et al. 1997) of 2048^3 particles within a $(1000\ \mathrm{Mpc}\ h^{-1})^3$ cube. The latest WMAP5 and WMAP7 cosmological parameters were used. This simulation is particularly well suited for our purpose because of its large number of clusters.

We use the MultiDark halo catalog from its on-line database,[3] constructed with the Bound Density Maxima algorithm (Klypin & Holtzman 1997). We will mainly use M_{500} and R_{500} for comparison with existing observational works. We use the technique described in Hu & Kravtsov (2003) to convert M_{200} and R_{200} provided by the MultiDark halo catalog to M_{500} and R_{500}. In creating our cluster sample we only select distinct halos, i.e., those halos that are not sub-halos of any other halo, which by definition are not galaxy clusters.

Additionally, we assume that the main emission mechanism in the ICM is thermal bremsstrahlung, which is true only above a particle energy of approximately 2.6 keV (Sarazin 1988). Below this energy, there could be other important contributions to the emission, e.g., from atomic lines. Therefore, we impose a mass cut of $M_{200} \geq 1\times10^{14}\ h^{-1}\ \mathrm{M}_\odot \approx 1.4\times10^{14}\ h_{70}^{-1}\ \mathrm{M}_\odot$ which ensures $k_\mathrm{B}T \gtrsim 2.6$ keV, assuming the $M_{500} - T_\mathrm{ci}$ relation of Mantz et al. (2010a).

The LOFAR radio observatory is expected to detect RHs up to redshift $z \approx 1$. Thus, we make use of different simulation snapshots up to $z = 1$. In Table 1, we show the total cluster number in our final cluster sample at different redshifts.

2.2. Gas density modeling

We decided to use a *phenomenological* approach and to construct the gas density profiles directly from X-ray observations.

---

[2] www.lofar.org

[3] www.multidark.org.

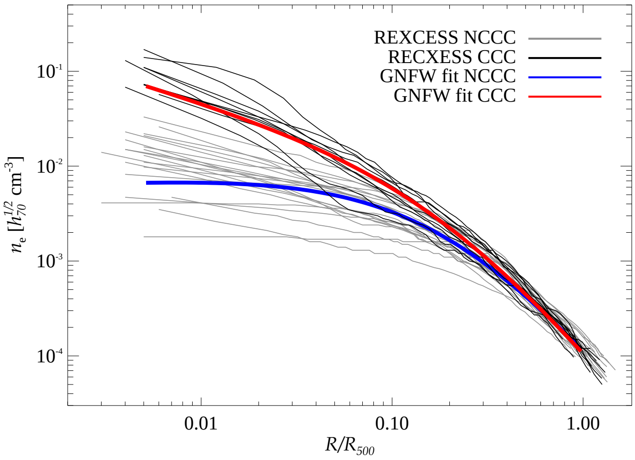

Fig. 1. Electron density profiles of the 31 clusters in the REXCESS sample. Grey and black lines represent NCCCs and CCCs, respectively. The blue and red lines represent our GNFW mean profile for the NCCCs and CCCs, respectively.

A suitable X-ray sample that provides the needed information is the *Representative XMM-Newton Cluster Structure Survey* (REXCESS) sample (Croston et al. 2008; Pratt et al. 2009). It is a sample of 31 galaxy clusters of different dynamical states at redshifts $0.06 < z < 0.18$ with detailed information on the de-projected electron density profiles (Croston et al. 2008). In Figure 1, we show the 31 electron density profiles of the REXCESS sample color-coded by CCCs and NCCCs.

In order to obtain an electron density profile that we will attach to our simulated clusters, we use a generalized Navarro-Frank-White (GNFW) profile,

$$n_e(x) = \frac{n_0}{x^\beta \left[1 + x^\alpha\right]^{\frac{\delta-\beta}{\alpha}}}, \tag{1}$$

where $x = R/R_c$ and R_c is the cluster core radius. To reduce the dimensionality of our fit, we fix representative values of $R_c = 0.2\,R_{500}$, $\alpha = 1$ and $\delta = 2.5$. We fit the radial density profiles of the REXCESS sample in log-log space, separating them in the two categories of NCCCs and CCCs as shown in Figure 1. We obtain $n_{0,\mathrm{NCCC}} = 1.02 \times 10^{-2}\ h_{70}^{1/2}\ \mathrm{cm}^{-3}$, $n_{0,\mathrm{CCC}} = 8.32 \times 10^{-3}\ h_{70}^{1/2}\ \mathrm{cm}^{-3}$, $\beta_{\mathrm{NCCC}} = -0.093$, and $\beta_{\mathrm{CCC}} = 0.592$. The resulting fits are shown in blue and red for the NCCC and CCC population, respectively.

The next step is to introduce a mass-scaling in order to apply our GNFW profiles to all our clusters. We adopt the gas mass fraction-mass scaling, $f_{\mathrm{gas},500} - M_{500}$ of Sun et al. (2009) (and adopt their Equation (8)). We can express $f_{\mathrm{gas},500}$ in the following way:

$$f_{\mathrm{gas},500} = \frac{M_{\mathrm{gas},500}}{M_{500}} = \frac{\int_0^{R_{500}} \rho_{\mathrm{gas}} \mathrm{d}V}{M_{500}} \tag{2}$$

with $\rho_{\mathrm{gas}}(R) = \rho_{\mathrm{gas}} = n_e m_p/(X_H X_e)$ where m_p is the proton mass, $X_H = 0.76$ is the primordial hydrogen mass fraction and $X_e = 1.157$ the ratio of electron-to-hydrogen number densities in the fully ionized ICM (Sarazin 1988). For each cluster i of our sample, we then define a *mass-scaled* gas profile as $\rho_{\mathrm{gas},i} = C_i\,\rho_{\mathrm{gas}}$ with:

$$C_i = (0.0656 \pm (0.0064 g_1))\,h_{70}^{-1.5} \times \left(\frac{M_{500,i}}{1.04 \times 10^{13} h_{70}^{-1} \mathrm{M}_\odot}\right)^{0.135 \pm (0.030 g_2)} \frac{M_{500,i}}{\int_0^{R_{500,i}} \rho_{\mathrm{gas}} \mathrm{d}V} \tag{3}$$

where g_1 and g_2 are random Gaussian number which we use in order to simulate the natural scatter of the gas profiles.[4]

Hence, for each cluster in our sample we obtain a gas density profile $\rho_{\mathrm{gas},i}$ that obeys the observed $f_{gas,500} - M_{500}$ relation and is uniquely determined by its DM mass $M_{500,i}$ and by the property of being a NCCC or CCC. We assign the latter property to every halo depending on its merging history. In particular, we make use of the offset parameter X_{off} computed for the MultiDark halo catalog. This is defined as the distance from the halo center to the center of mass in units of the virial radius. This parameter assesses the dynamical state of the cluster and whether the halo experienced a recent merger or not. Current observations reveal a ratio of NCCCs and CCCs of about 50% (see, e.g., Chen et al. 2007; Sanderson et al. 2009). Since there is a correlation between merging clusters and NCCCs, we use the median of the X_{off} distribution to separate our sample into CCCs and NCCCs (with NCCCs defined to be those halos with the larger dynamical offsets). Clearly, this is an over-simplification, and future X-ray surveys will have to determine this property also as a function of redshift.

We also account for redshift evolution of the gas profiles. While our NCCC and CCC gas profiles as derived from the REXCESS cluster sample are merely used to define a profile shape, the normalization of the gas profiles is set by the observational $f_{\mathrm{gas},500} - M_{500}$ relation (Sun et al. 2009). The 43 clusters used in Sun et al. (2009) have redshifts $0.012 < z < 0.12$ with a *median* of $z \approx 0.04$. Thus, our phenomenological gas profile is representative of the cluster population at $z \approx 0$. To extend this profile to high-z, we include a *self-similar* scaling of the gas density as $\rho_{\mathrm{gas}}(z) = E(z)^2 \rho_{\mathrm{gas}}(z = 0)$, where $E(z)^2 = \Omega_m (1+z)^3 + \Omega_\Lambda$.

2.3. X-ray and SZ scaling relations

In order to check whether our phenomenologically derived gas profiles reproduce the observations, we calculate the bolometric X-ray thermal bremsstrahlung luminosity L_{bol} as in Sarazin (1988)[5] and compare our sample result with the observed $L_{\mathrm{bol}} - M_{500}$ relation and XLF.[6]

To assign a temperature to our model clusters (that is needed for calculating L_{bol} and Y_X), we adopt the $T - M_{500}$ relation by Mantz et al. (2010a),

$$\log_{10}\left(\frac{k_B T_{\mathrm{ci}}}{\mathrm{keV}}\right) = A + B\ \log_{10}\left(\frac{E(z) M_{500}}{10^{15} h_{70}^{-1} \mathrm{M}_\odot}\right) \tag{4}$$

---

[4] The values 0.0064 and 0.03 quoted in Equation (3) do not represent the proper scatter of the $f_{\mathrm{gas},500} - M_{500}$ relation but reflect the parameter errors and we rescaled the numerical values to a Hubble constant of h_{70} used in this work.

[5] We check our procedure by fitting each of the 31 REXCESS clusters with Equation (1) and calculating L_{bol} with the measured gas temperature of each cluster. As a result, we fall short of the observed luminosity by a mean (median) of about 21% (20%). This is reasonable considering that we do not permit the parameters R_c, α and δ to vary between different objects. Additionally, we neglect atomic line emission which may give a noticeable contribution, in particular for low-mass clusters and in the cluster outskirts of larger systems.

[6] The mean (median) difference at $z = 0$ between L_{bol} within R_{200} or within R_{500} is ≈ 5% (≈ 7%). While L_{bol} refers to the quantity calculated within R_{500}, we note that the XLF for luminosities calculated within R_{200} will be barely changed.

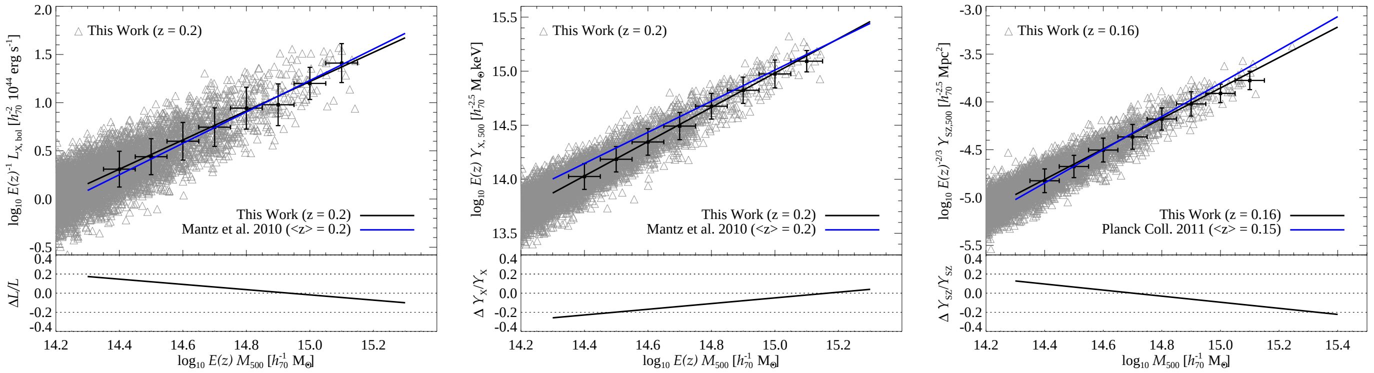

Fig. 2. X-ray and SZ scaling relations. Grey triangles show the MultiDark sample (limited to the mass range covered by observations), the black line is the corresponding scaling relation, and the blue line is the observational result. The black crosses represent the median values of the quantity in question for a given mass bin (indicated by horizontal error bars), and the vertical error bars represent the standard deviation within a bin. *Left.* We compare the bolometric X-ray luminosity-to-mass relation, $L_{\rm bol} - M_{500}$, at $z = 0.2$ to the observational sample by Mantz et al. (2010a) with a median of $z \approx 0.2$. *Center.* $Y_{\rm X} - M_{500}$ scaling relation of our model in comparison to the observational sample by Mantz et al. (2010a). *Right.* $Y_{\rm SZ} - M_{500}$ scaling relation at $z = 0.16$ in comparison to the observational sample by the Planck Collaboration et al. (2011) with a median redshift of about 0.15. The bottom panels show the relative difference to the observational scaling relations.

where $A = 0.91$, $B = 0.46$, and $T_{\rm ci}$ is the cluster temperature *not* centrally excised (see Mantz et al. 2010a). Mantz et al. (2010a) report a scatter of $\sigma_{\rm yx} = 0.06$,[7] which we apply to our sample using Gaussian deviates.

In the left panel of Figure 2, we show how our model $L_{\rm bol} - M_{500}$ relation compares with observations by Mantz et al. (2010a) (*all* data, see their Table 7). Their sample is composed of 238 clusters at $0.02 < z < 0.46$ with a median of $z \approx 0.2$ and self-consistently takes into account all selection effects, covariances, systematic uncertainties and the cluster mass function (Mantz et al. 2010b). For this reason, we compare the Mantz et al. (2010a) data to our model at $z = 0.2$, and limit the comparison to the mass range covered by the observations. Overall, there is reassuring agreement between our phenomenological model and the data, which probe our model most closely on scales around the cluster core radii (which is where the contribution to $L_{\rm X}$ per logarithmic interval in radius, $\mathrm{d}L_{\rm X}/\mathrm{d}\log r \propto r^3 n_{\rm gas}^2(r)\sqrt{k_{\rm B}T}$, attains its maximum). In Table 2, we show our model $L_{\rm bol} - M_{500}$ scaling relation and its scatter for different redshifts. We find that the scatter of our samples at all redshifts are Gaussian distributed with a standard deviation of $\sigma_{yx} \approx 0.18$ that matches the observational results of Mantz et al. (2010a), which report a scatter of $\sigma_{yx} = 0.185$.

In the middle panel of Figure 2, we compare the $Y_{\rm X} - M_{500}$ relation of our sample to observational data (Mantz et al. 2010a). The model agrees nicely at the high-mass end, but underpredicts the observed scaling at low masses by about 20% (at the 1-σ level). This is the same level of deviation from the data as in the case of $L_{\rm X}$, which is more significant due to the smaller scatter in the $Y_{\rm X}$ relation. The differential contribution to the thermal energy per logarithmic interval in radius (and hence to the integrated Compton-y parameter) is given by $\mathrm{d}Y/\mathrm{d}\log r \propto r^3 P_{\rm th}(r)$, with the thermal gas pressure $P_{\rm th} = n_{\rm gas}k_{\rm B}T$. It peaks at scales slightly smaller than R_{500} with 1-σ contributions extending out to $3\,R_{500}$ (Battaglia et al. 2010). Hence, the observational scaling constrains our model on those large scales, quite complementary to the X-ray luminosity. The deviations at small masses either indicates different assumptions about $f_{\rm gas}$, the gas temperature, or different selection effects of either observational sample that we use for model calibration and comparison. Mantz et al. (2010a) determine their masses by adopting a constant value for $f_{\rm gas}$, in contrast to our approach which adopts the observed $f_{\rm gas,500} - M_{500}$ relation given by Sun et al. (2009). Additionally, we adopt the Mantz et al. (2010a) *centrally included* temperature throughout all our work, while Mantz et al. (2010a) use the *centrally excised* temperature to calculate $Y_{\rm X}$. This assumption also impacts the scatter of the $Y_{\rm X} - M$ relation. In fact, using the *centrally included* temperature, we found a scatter of $\sigma_{yx} \approx 0.11$ (see Table 3 where our $Y_{\rm X}$ scaling relations are reported), significantly higher than the value of $\sigma_{yx} = 0.052$ found by Mantz et al. (2010a).

In the right panel of Figure 2, we compare the $Y_{\rm SZ} - M_{500}$ relation in our model (calculated as in Equation (3) of Battaglia et al. 2011) with the observed scaling relation by the Planck Collaboration et al. (2011). Their sample contains clusters up to $z \approx 0.45$ and has a median of $z \approx 0.15$; hence, we compare the data to our relation at the MultiDark snapshot $z = 0.16$ (that contains 11419 clusters above our mass cut) which however is not used throughout the rest of the work. Our model reproduces the data remarkably well, except for the high-mass end where our simulations have a weaker constraining power due to the smaller box size in comparison to the survey volume of *Planck*. We find a scatter of $\sigma_{yx} \approx 0.11$ which compares well with the *Planck* result of $\sigma_{yx} \approx 0.1$. In Table 4, we report our SZ scaling relations for different redshifts.

2.4. X-ray luminosity function

Studies of the XLF got out of fashion during the last years due to the difficulties of using the X-ray luminosity for cosmological purposes. The X-ray emissivity scales with the square of the gas density, which makes it subject to density variations and clumping. This implies large scatter that causes a large Malmquist bias and underlines the necessity of careful mock surveys that need to address all systematics.

---

[7] Scatter is calculated as $\sigma_{\rm yx} = \sqrt{\left\{\Sigma_{i=1}^{N}[Y_i - (A + B\,X_i)]^2\right\}/N - 1}$ where the sum extends over the data points X_i, Y_i, and A and B are the fit parameters.

Table 2. $L_{\rm bol} - M_{500}$ scaling relations.

redshift z	A	B	σ_{yx}
0	-21.41 ± 0.11	1.50 ± 0.01	0.179
0.1	-21.30 ± 0.12	1.50 ± 0.01	0.179
0.2	-21.50 ± 0.13	1.51 ± 0.01	0.178
0.4	-21.13 ± 0.17	1.49 ± 0.01	0.178
0.61	-21.59 ± 0.22	1.53 ± 0.01	0.177
0.78	-20.73 ± 0.29	1.48 ± 0.02	0.177
1	-20.45 ± 0.42	1.46 ± 0.03	0.177

Note. Scaling relations are reported in the form of $\log_{10}\ (L_{\rm bol}\ /\ E(z)\ h_{70}^{-2}\ 10^{44}\ {\rm erg\ s}^{-1}) = A + B\ \log_{10}\ (E(z)\ M_{500}\ /\ h_{70}^{-1}\ {\rm M}_{\odot})$. The relation scatter σ_{yx} is also shown.

Table 3. $Y_{\rm X,500} - M_{500}$ scaling relations.

redshift z	A	B	σ_{yx}
0	-9.18 ± 0.07	1.61 ± 0.01	0.109
0.1	-8.85 ± 0.07	1.59 ± 0.01	0.109
0.2	-8.82 ± 0.08	1.59 ± 0.01	0.109
0.4	-8.79 ± 0.10	1.59 ± 0.01	0.108
0.61	-8.65 ± 0.14	1.59 ± 0.01	0.109
0.78	-8.36 ± 0.18	1.57 ± 0.01	0.109
1	-8.28 ± 0.26	1.57 ± 0.02	0.109

Note. Scaling relations are reported in the form of $\log_{10}\ (E(z)\ Y_{\rm X,500}\ /\ h_{70}^{-2.5}\ {\rm M}_{\odot}\ {\rm keV}) = A + B\ \log_{10}\ (E(z)\ M_{500}\ /\ h_{70}^{-1}\ {\rm M}_{\odot})$. The relation scatter σ_{yx} is also shown.

Table 4. $Y_{\rm SZ,500} - M_{500}$ scaling relations.

redshift z	A	B	σ_{yx}
0	-27.93 ± 0.07	1.60 ± 0.01	0.109
0.1	-27.74 ± 0.07	1.59 ± 0.01	0.109
0.16	-27.76 ± 0.08	1.59 ± 0.01	0.109
0.2	-27.65 ± 0.08	1.59 ± 0.01	0.109
0.4	-27.57 ± 0.10	1.59 ± 0.01	0.108
0.61	-27.50 ± 0.13	1.59 ± 0.01	0.109
0.78	-27.15 ± 0.18	1.58 ± 0.01	0.109
1	-27.01 ± 0.26	1.58 ± 0.02	0.109

Note. Scaling relations are reported in the form of $\log_{10}\ (E(z)^{-2/3}\ Y_{\rm SZ,500}\ /\ h_{70}^{-2.5}\ {\rm Mpc}^2) = A + B\ \log_{10}\ (E(z)\ M_{500}\ /\ h_{70}^{-1}\ {\rm M}_{\odot})$. The relation scatter σ_{yx} is also shown.

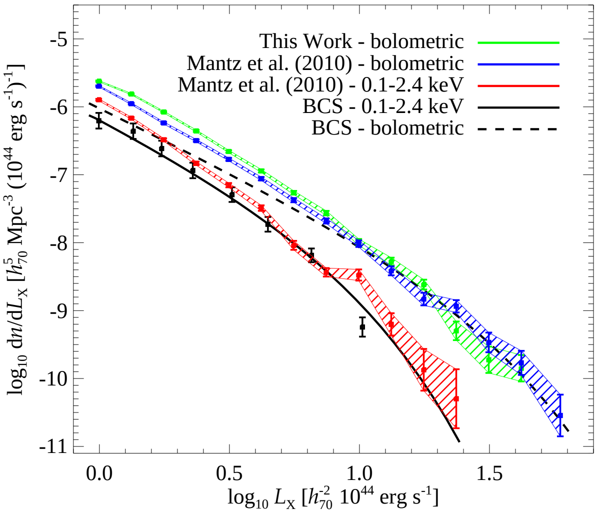

Fig. 3. Bolometric and soft-band ($0.1 - 2.4$ keV) XLFs. Shown are the soft-band data points, the soft-band and bolometric Schechter fits of the BCS sample of Ebeling et al. (1997), which has a median of $z \approx 0.08$. While the soft-band XLF, which was obtained applying the Mantz et al. (2010a) $L_{\rm X} - M_{500}$ relation to the MultiDark $z = 0.1$ snapshot, compares well with the BCS data points, it deviates from the corresponding Schechter fit. We also show the bolometric XLF of Mantz et al. (2010a) and bolometric XLF of our model at $z = 0.1$. The XLFs are calculated in equally log-spaced mass bins; the error bars represent the Poissonian errors. Note that we limit the comparison to the luminosity range covered by our sample, where we cut the lowest part because in that range the XLF rapidly drops due to the imposed mass cut.

Nevertheless, it provides a complementary check for our model. To this end, we use the *ROSAT* brightest cluster sample (BCS) XLF (Ebeling et al. 1997), which is in good agreement with results from the *ROSAT* ESO Flux-Limited X-ray (REFLEX; Böhringer et al. 2002) and HIFLUGCS (Reiprich & Böhringer 2002). Note that the XLF is fully determined by the mass function and the $L_{\rm X} - M_{500}$ relation after taking into account the observational biases. This means that applying the Malmquist and Eddington bias corrected $L_{\rm X} - M_{500}$ relation by Mantz et al. (2010a) directly to the MultiDark mass function and accounting for the observational scatter in $L_{\rm X} - M_{500}$ should yield an unbiased XLF. We show the resulting bolometric and soft-band ($0.1 - 2.4$ keV) XLF in Figure 3 and compare those to the corresponding BCS XLFs and to our model predictions. Note that there is only the Schechter fit available for the BCS bolometric XLF. While the soft-band XLF by Mantz et al. (2010a) agrees well with the BCS data points, it deviates from the corresponding Schechter fit at low luminosities. This is also true in the bolometric band, where the XLFs of Mantz et al. (2010a) and our model agree well, but deviate from the BCS Schechter fit at low luminosities. This may be an artifact due to the use of Schechter fit instead of the data points or may point to incompleteness of the BCS sample. Note that the Poissonian errors of the XLF obtained from the MultiDark simulation are a lower limit as we are neglecting the uncertainty due to cosmic variance. Studies of the XLF will become again an important topic with the upcoming launch of the eROSITA satellite (see, e.g., Cappelluti et al. 2011) and further studies in this direction are desirable. For these reasons, we do not show XLF predictions at other redshifts, leaving this for a future study.

Summarizing, our phenomenological approach provides viable gas densities that reproduce the observed scaling relations of the ICM as well as the XLF. Thus, we will apply it in the following to model the CR population in galaxy clusters and to predict the radio and gamma-ray emission of our sample.

2.5. Cosmic ray modeling

We assume a power-law for the CR proton distribution, $f(R, p){\rm d}p = C(R)p^{-\alpha}{\rm d}p$, which is the effective one-dimensional momentum distribution (assuming isotropy in momentum space). We are interested in calculating the radio synchrotron (and gamma-ray) emission resulting from secondaries of hadronic CR interactions with protons of the ICM. To start, we provide the synchrotron emissivity j_ν, at frequency ν and per steradian, of a steady-state electron population where radiative cooling balances injection from hadronic interactions (adapted from Pfrommer et al. 2008 and Enßlin et al. 2011),

$$j_\nu = A_\nu C(R) \rho_{\rm gas}(R) \frac{\epsilon_{\rm B}(R)}{\epsilon_{\rm B}(R) + \epsilon_{\rm CMB}} \left(\frac{\epsilon_{\rm B}(R)}{\epsilon_{B_{\rm c}}} \right)^{(\alpha-2)/4}, \tag{5}$$

where the abbreviations A_ν and $\epsilon_{B_{\rm c}}$ are defined in Appendix B. $\epsilon_{\rm CMB}$ is the energy density of the cosmic microwave background (CMB), and $\epsilon_B = B^2/(8\pi)$ denotes the magnetic energy density. We assume a scaling of the magnetic field with gas density that is given by

$$B(R) = B_0 \left(\frac{\rho_{\rm gas}(R)}{\rho_{\rm gas,0}} \right)^{\alpha_B}, \tag{6}$$

where B_0 is the central magnetic field and $\alpha_{\rm B}$ describes the declining rate of the magnetic field strength toward the cluster outskirts. Such a parametrization is suggested by cosmological simulations (Dubois & Teyssier 2008) as well as Faraday rotation measurements (Bonafede et al. 2010; Kuchar & Enßlin 2011, and references therein). The radio surface brightness $S_\nu(R_\perp)$ (in the small-angle approximation) and luminosity L_ν, at a given frequency ν, are given by

$$S_\nu(R_\perp) = 2 \int_{R_\perp}^{\infty} j_\nu(R) \frac{R}{\sqrt{R^2 - R_\perp^2}} {\rm d}R, \tag{7}$$

$$L_\nu = 4\pi \int {\rm d}V j_\nu(R). \tag{8}$$

The flux is given by $F_\nu = L_\nu/(4\pi D^2)$ where D is the luminosity distance to the object. Note that we do not convolve S_ν with the instrumental point spread function unless specified.

The spatial CR distribution within galaxy clusters is governed by an interplay of advection, CR streaming and diffusion. The advection of CRs by turbulent gas motions is dominated by the largest eddy turnover time $\tau_{\rm tu} \sim L_{\rm tu}/\upsilon_{\rm tu}$. $L_{\rm tu}$ denotes the turbulent injection scale (typically of order the core radius) and $\upsilon_{\rm tu}$ is the associated turbulent velocity that gets close to the sound speed $\upsilon_{\rm s}$ for transsonic turbulence after a cluster merger and relaxes to small velocities afterwards. In contrast, the crossing time of streaming CRs over $L_{\rm tu}$ is $\tau_{\rm st} \sim \chi_B L_{\rm tu}/\upsilon_{\rm st}$ with the streaming velocity given by $\upsilon_{\rm st} \sim \upsilon_{\rm s}$ and $\chi_B \lesssim 1$ parametrizes the magnetic bending scale. Magnetic bottlenecks for the macroscopic, diffusive CR transport, are critical in lowering the microscopic streaming velocity of CR by some finite factor. Therefore, we can define a turbulent propagation parameter

$$\gamma_{\rm tu} \equiv \frac{\tau_{\rm st}}{\tau_{\rm tu}} = \frac{\chi_B \upsilon_{\rm tu}}{\upsilon_{\rm st}} \tag{9}$$

that indicates the relative importance of advection versus CR streaming as the dominant CR transport mechanism. After a merger, turbulent advective transport dominates yielding $\gamma_{\rm tu} \gg 1$, which results in centrally enhanced CR profiles. In contrast, in a relaxed cluster, CR streaming should be the dominant transport mechanism implying $\gamma_{\rm tu} \sim 1$ and producing flat CR profiles (for a detailed discussion of these processes, see Enßlin et al. 2011).

What we propose here is to keep the spectral shape of the CR distribution function as determined from cosmological hydrodynamical simulation of clusters (Pinzke & Pfrommer 2010), which however did not account for CR streaming. Hence the spatial CR distribution has to be modified to include the effects of CR streaming. For this reason we adopt the analytical result from Enßlin et al. (2011). This yields a model that includes the necessary CR transport physics and is able to predict the radio and gamma-ray emission while reproducing the observed RH properties. Note that this approach is not fully self-consistent and points to the necessity of future hydrodynamical simulations to include the effect of CR streaming and diffusion on the CR spectrum.

To construct such a model, we have to generalize the approach proposed by Enßlin et al. (2011) in order to account for GNFW gas profiles (Section 2.2). We also have to include the cluster mass-scaling of the CR normalization obtained from simulations (Pinzke & Pfrommer 2010). While details are given in Appendix A, we show below the main steps. When turbulent advection completely dominates the CR transport, the CR normalization can be written as (Enßlin et al. 2011)

$$C_{\rm adv}(R) = C_0 \left(\frac{P_{\rm th}(R)}{P_{\rm th,0}} \right)^{\frac{\beta_{\rm CR}}{\gamma}} = C_0 \eta(R)^{\beta_{\rm CR}}, \tag{10}$$

where $\beta_{\rm CR} = (\alpha + 2)/3$, $\gamma = 5/3$. We introduced the advective CR profile $\eta(R) = (P(R)/P_0)^{1/\gamma}$. Solving the continuity equation for CRs, Enßlin et al. (2011) derive the CR density profile,

$$\rho_{\rm CR}(R) = \rho_{\rm CR,0} \eta(R) \exp\left(\frac{R}{R_*} \right), \tag{11}$$

where $R_* = \gamma_{\rm tu} R_{\rm c}$ and $R_{\rm c}$ is the characteristic radius, of order the core radius, at which the turbulence is supposed to be injected. Now, we introduce the *semi-analytical* mass-dependent normalization of the CR profile of Pinzke & Pfrommer (2010) such that

$$\eta(R) = \left(\frac{C_{\rm adv}(R)}{C_0} \right)^{1/\beta_{\rm CR}} \rightarrow \left(\frac{C_{\rm hybrid}(R)}{C_0} \right)^{1/\beta_{\rm CR}}, \tag{12}$$

which effectively redefines $C_{\rm adv}(R)$ by that of our hybrid model, i.e.,

$$C_{\rm hybrid}(R) = \tilde{C}(R) \frac{\rho_{\rm gas}(R)}{m_{\rm p}} \frac{T(R)}{T_0}. \tag{13}$$

Here, $\tilde{C}(R)$ is the normalization CR profile of Equation (22) of Pinzke & Pfrommer (2010). We additionally account for the temperature decline toward the cluster periphery, $T(R)$, given by the fit to the universal temperature profile obtained from cosmological hydrodynamical simulations (Pfrommer et al. 2007; Pinzke & Pfrommer 2010) and deep *Chandra* X-ray observations (Vikhlinin et al. 2005). Eventually, the CR profile in our hybrid model is $C(R) = C_0(\rho_{\rm CR}(R)/\rho_{\rm CR,0})^{\beta_{\rm CR}}$ within $R_\pm$ of Equation (A.2), with $\rho_{\rm CR}$ defined by Equation (11) where $C_{\rm hybrid}$ enters through our redefinition of η, and $C(R) = C(R_\pm)$ for $R > R_+$ and $R < R_-$, respectively.

The last step is to generalize the case of one CR population with a single spectral index α to include the spectral curvature as suggested by Pinzke & Pfrommer (2010). They model the CR spectrum with three different power-law CR populations with spectral indices of $\alpha_i = (2.15, 2.3, 2.55)$. Our formalism can be easily extended to account for multiple CR populations by extending the terms with a single α to sums over the three spectral indices (see Pinzke & Pfrommer 2010). This extension has to be applied to A_ν, to the factor $(\epsilon_{\rm B}(R)/\epsilon_{B_{\rm c}})^{(\alpha-2)/4}$ of Equation (5), and to Equation (10). While the modifications are straight forward in the first two cases (and are adopted for our hybrid model, see

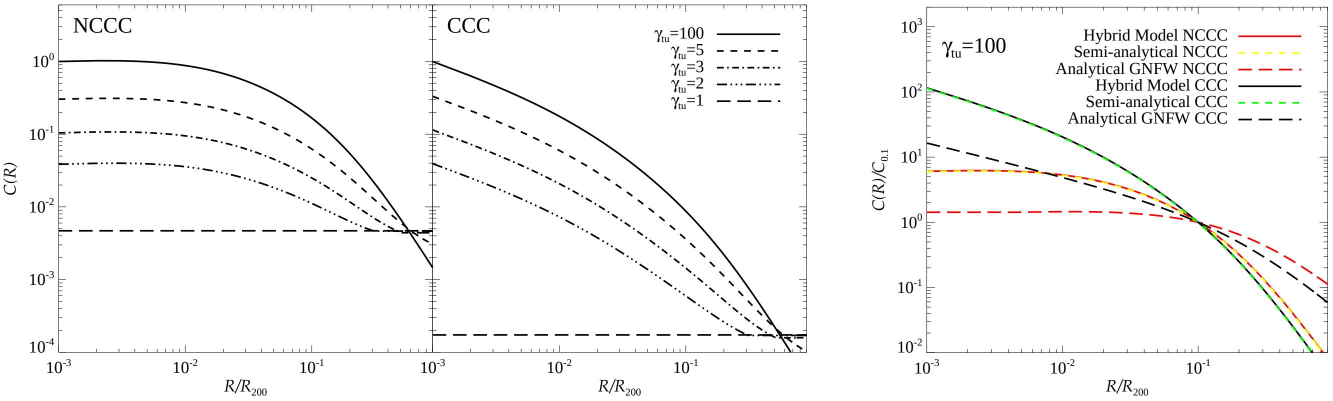

Fig. 4. *Left panel.* We show our hybrid model profiles for the normalization of the CR distribution for the NCCC and CCC cases and for different values of $\gamma_{\rm tu}$. We fix the CR number for the case of $\gamma_{\rm tu} = 100$ using Equation (36) of Enßlin et al. (2011), while integrating the cluster volume within R_{200}, and require CR number conservation during CR streaming. *Right panel.* We compare the hybrid model (adopting $\gamma_{\rm tu} = 100$) with the semi-analytical advection-only case (adopting our GNFW gas profiles and the outer temperature decrease to the simulation-derived model proposed by Pinzke & Pfrommer 2010) and with the exact analytical solution as in Enßlin et al. (2011), but for our GNFW profiles (adopting $\alpha = 2.3$ and $\gamma_{\rm tu} = 100$). Here, the CR profiles are normalized at $C_{0.1} = C(0.1R_{200})$.

Appendix B), introducing a sum over α_i in Equation (10) would make impossible to solve analytically for $\eta(R)$ in Equation (12). For simplicity, we decided to only use $\alpha = 2.3$ in this last case.[8] For the highly turbulent cases, i.e., for $\gamma_{\rm tu} = 100$ (1000), we recover the radial shape and normalization of the semi-analytical model of Pinzke & Pfrommer (2010) within 1% (0.1%).

Summarizing, our *hybrid* model for the CR distribution function, has the following properties: it accounts for (i) the X-ray-inferred (CCC and NCCC) gas profiles and cluster-mass scaling of the gas fraction, in addition to the universal temperature drop in the outskirts of clusters, (ii) a cluster-mass dependent CR normalization and universal CR spectrum as derived from cosmological hydrodynamical simulations, (iii) an effective parametrization of active CR transport processes, including CR streaming and diffusion, which allows us to explore different turbulent states of the clusters in our MultiDark sample.

In the left two panels of Figure 4, we show our hybrid CR normalization for the NCCC and CCC cases and for different values of $\gamma_{\rm tu}$. As expected, when CR streaming is the dominant CR transport mechanism, i.e., for negligible advective turbulent transport or equivalently, $\gamma_{\rm tu} \sim 1$, the spatial CR profiles are flattened irrespective of the cluster state. While turbulence in NCCCs could be injected by a merging (sub-)cluster, in the case of CCCs, the interaction of the AGN jet or radio lobe with the ambient ICM could be the source of turbulence.

In the right panel of Figure 4, we compare our hybrid model profile with the semi-analytical advection-only case (adopting our GNFW gas profiles and the outer temperature decrease to the model proposed by Pinzke & Pfrommer 2010) and with the exact analytical solution as in Enßlin et al. (2011), but for our GNFW profiles (see Appendix A for details). The profiles are normalized at $0.1R_{200}$. In that case of dominant advective CR transport, our hybrid model compares nicely with the semi-analytical model derived from cosmological cluster simulations (Pinzke & Pfrommer 2010). The main differences between our hybrid model (and the semi-analytical model) on the one side and the analytical solution on the other side is the inclusion of the simulation-based "reference" profile $\tilde{C}$ for the advection-only case and the universally observed temperature drop towards the outskirts of clusters. Note that the profiles in our hybrid model are generally more centrally peaked in comparison to the analytical GNFW case, which is due to the enhanced radiative cooling in the Pinzke & Pfrommer (2010) simulations that did not account for AGN feedback. Thanks to the flexible parametrization in our model, this can be easily counteracted by changing $\gamma_{\rm tu}$ and α_B, however, at the expense that these parameters are now degenerate with our assumptions on the CR profile in the advection-dominated regime and other possible effects that we are not considering such as cluster asphericity (see also next Section 3).

3. Radio Surface Brightness Modeling

In this Section we apply our model to reproduce the emission characteristics of four well-observed RHs. Hence for the purpose of this section, we adopt the measured gas and temperature profiles derived from X-ray observations of each cluster. Our hybrid model includes an overall normalization $g_{\rm CR}$ of the CR distribution function and the hadronically-induced non-thermal emission (see Appendix B). Note that this parameter can be interpreted as a functional that depends on the *maximum CR acceleration efficiency*, $g(\zeta_{\rm p,max})$, (Pinzke & Pfrommer 2010) but *only* for $\gamma_{\rm tu} \gtrsim 100$. We will additionally study the CR-to-thermal pressure $X_{\rm CR} = P_{\rm CR}/P_{\rm th}$, where the CR pressure is given by

$$P_{\rm CR} = \frac{g_{\rm CR} C m_{\rm p} c^2}{6} \sum_{i=1}^{3} \Delta_i \mathcal{B}_{1/(1+q^2)}\left(\frac{\alpha_i - 1}{2}, \frac{3-\alpha_i}{2}\right). \tag{14}$$

Here, c is the speed of light, $q = 0.8$ is the low-momentum cutoff of the CR distribution, and the normalization factors of the individual CR populations are given by $\Delta_i = (0.767, 0.143, 0.0975)$ (Pinzke & Pfrommer 2010, see also Appendix B).

3.1. Modelling individual radio halos

For our study, we choose the giant radio halos of Coma (Deiss et al. 1997) and Abell 2163 (Feretti et al. 2001;

---

[8] We checked that the choice of α in Equation (10) has only a minor effect on the results. Varying α within 2.15 − 2.55 leaves the radial shape and the normalization unchanged within 0.5%.

Murgia et al. 2009), both in merging NCCCs, and the radio mini-halos of Perseus (Pedlar et al. 1990) and Ophiuchus (Govoni et al. 2009; Murgia et al. 2009), both in relaxed CCCs. The radio emission of these clusters is representative of a wide class of RHs. Additionally, Perseus, Ophiuchus and Coma are among the most promising clusters for gamma-ray observations (Pinzke & Pfrommer 2010; Pinzke et al. 2011). In Table 5, we summarize the main characteristics of these halos and detail the main parameters adopted for the modeling and the corresponding results. In Figure 5, we show the surface brightness and CR-to-thermal pressure profile of each cluster. We model these clusters at 1.4 GHz and within R_{200}.

3.1.1. The Coma radio halo

The giant radio halo in Coma has a morphology remarkably similar to the extended X-ray thermal bremsstrahlung emission, although the radio emission declines more slowly towards the cluster outskirts (Briel et al. 1992; Deiss et al. 1997). Note that the morphology is non-spherical, showing an elongation in the East-West direction. The full-width half maximum (FWHM) of the radio beam is 0.156 deg (Deiss et al. 1997), almost two orders of magnitude larger than the X-ray observation of Briel et al. (1992).[9] Thus, we apply a Gaussian smoothing to our theoretical surface brightness of Equation (7) with $\sigma_{\mathrm{smoothing}} = FWHM_{\mathrm{radio}}/2.355$.

We investigate different values for $\alpha_{\mathrm{B}} = (0.3, 0.4, 0.5, 0.6, 0.7)$ and for γ_{tu} ranging from 1 to 100. First, we fix the CR number for $\gamma_{\mathrm{tu}} = 100$ using Equation (36) of Enßlin et al. (2011) while integrating the cluster volume within R_{200}. Then, we require CR number conservation during CR streaming (for CR energies $E >$ GeV where Coulomb cooling is negligible for CR protons), i.e., when lowering the values of γ_{tu}. Fixing the central magnetic field $B_0 = 5\ \mu$G (Bonafede et al. 2010), we use g_{CR} as normalization factor to match the radio observations. The best match to the data is obtained for $\gamma_{\mathrm{tu}} = 1$ and $\alpha_{\mathrm{B}} = 0.6$. Values as high as $\gamma_{\mathrm{tu}} \approx 4$ can be accommodated, however, at the expense of a shallower decline of the magnetic field profile (smaller α_B) as a function of cluster-centric radius. We recover the radio surface brightness shape and the total radio luminosity within about 20%.

The gamma-ray flux (see Appendix C) within R_{200} for the $\gamma_{\mathrm{tu}} = 1$ case and for energies above 100 MeV (100 GeV) is $F_\gamma = 4.1 \times 10^{-9}$ (1.5×10^{-12}) cm^{-2} s^{-1}. Hence, it is in tension with the limit recently set by *Fermi*-LAT (Zimmer et al. 2012) of $F_{\gamma,UL}(> 100\ \mathrm{MeV}) \approx 2.5 \times 10^{-9}$ cm^{-2} s^{-1}. Note that for slightly higher values of γ_{tu}, i.e., a more centrally concentrated CR distribution, the radio and gamma-ray yield would be increased (assuming CR number conservation). However, in order to match the observed radio synchrotron profiles, we have to decrease the CR normalization (parametrized by g_{CR}). This causes the associated gamma-ray flux also to be reduced to a level that is low enough to easily circumvent the gamma-ray constraints. In fact, for $\gamma_{\mathrm{tu}} = 4$, we obtain $F_\gamma(> 100\ \mathrm{MeV}) = 9.6 \times 10^{-10}$ cm^{-2} s^{-1} (and $F_\gamma(> 100\ \mathrm{GeV}) = 3.6 \times 10^{-13}$ cm^{-2} s^{-1}). We caution that in principle, CR streaming should cause the CR spectrum to steepen. This may then considerably weaken these constraints as a result of the convex spectral curvature since the gamma-ray emission probes the high-energy tail of the CR distribution that is suppressed in this picture in comparison to the lower-energy protons that the radio emission is sensitive to (see Aleksić et al. 2012, for an extended discussion of this point).

Note that this analysis confirms the result by Arlen et al. (2012) who also conclude that the hadronic model for the Coma radio halo is an attractive explanation for magnetic field estimates inferred by Faraday rotation measure studies (Bonafede et al. 2010) and is not challenged by *Fermi* upper limits on the gamma-ray emission if the full range of CR spectral indices is considered, i.e., for $2.1 \lesssim \alpha \lesssim 2.5$. Pfrommer & Enßlin (2004a) demonstrate that those spectral indices provide a fair description of the radio emission after taking into account the negative flux bowl due to the SZ effect that causes the measured radio halo spectrum to experience a sharp cutoff towards high frequencies.

This is not necessarily in conflict with results by Brunetti et al. (2012) who point out problems of the hadronic model for the *limited* parameter space $\alpha \gtrsim 2.6$, while adopting a slightly shallower azimuthally averaged radio halo profile (Brown & Rudnick 2011) than the one used in this analysis (Deiss et al. 1997). Careful work is needed to understand the origin of the observational discrepancy and to cleanly separate the radio halo emission from that of the Coma radio relic and other sources in the field. Interestingly, Brunetti et al. (2012) need very flat CR profiles both for their hadronic and re-acceleration models in order to reproduce the Coma surface brightness which corresponds to our finding.

3.1.2. The radio halo in Abell 2163

The morphology of the giant radio halo in Abell 2163 is also closely correlated to the cluster thermal X-ray structure. As in Coma, the radio emission declines towards the cluster outskirts at a slower rate in comparison to the thermal X-ray emission (Feretti et al. 2001). The morphological appearance is non-spherical, with an elongation in the East-West direction. We use the surface brightness map provided by Murgia et al. (2009) for which the synthesized radio beam can be approximated by a circular Gaussian with $FWHM_{\mathrm{radio}} = 62''$. Again, $FWHM_{\mathrm{radio}}$ is larger than the resolution of the *ROSAT* observation and the corresponding gas density profile. Converted to physical scale, $\sigma_{\mathrm{smoothing}}$ is of the order of that in Coma because of the larger distance of Abell 2163. Hence, we also apply Gaussian smoothing.

We follow the same procedure as in Coma, and adopt a central magnetic field strength of $B_0 = 5\ \mu$G. The only match to the data is obtained for $\gamma_{\mathrm{tu}} = 1$ and $\alpha_B = 0.3$, i.e., the flattest possible surface brightness. We recover the emission shape and the total luminosity within about 15%. The corresponding gamma-ray flux within R_{200} is $F_\gamma(> 100\ \mathrm{MeV}) = 4.2 \times 10^{-10}$ cm^{-2} s^{-1}, about two orders of magnitude lower than the upper limit obtained by *Fermi*-LAT (Ackermann et al. 2010a), and $F_\gamma(> 100\ \mathrm{GeV}) = 1.5 \times 10^{-13}$ cm^{-2} s^{-1}.

3.1.3. The Perseus radio mini-halo

The diffuse radio emission in Perseus is the best known example of a radio mini-halo (Pedlar et al. 1990) and Perseus itself is among the best studied clusters in X-rays (e.g., Churazov et al. 2003; Fabian et al. 2006, 2011). Also the Perseus radio morphology resembles that in the X-rays. We proceed as before, but now adopt a higher central magnetic field strength of $B_0 = 10\ \mu$G. Such a larger B_0 is expected in a CCC with its higher central gas density, implying a larger adiabatic compression factor of

---

[9] Note that the apparent displacement of the radio and X-ray peak of about 0.05 deg is well within the angular resolution of the radio observation and hence negligible for the modeling.

Table 5. Radio-halo and mini-halo characteristics.

name	z	D	Δd	$L_{1.4\text{ GHz, obs}}$	model parameters	$L_{1.4\text{ GHz, model}}$	references
		$[h_{70}^{-1}$ Mpc]	$[h_{70}^{-1}$ Mpc]	10^{31} $[h_{70}^{-2}$ erg s^{-1} Hz$^{-1}]$	γ_{tu}, α_{B}	10^{31} $[h_{70}^{-2}$ erg s^{-1} Hz$^{-1}]$	
Coma	0.023	101	2.15	0.72	1, 0.6	0.86	[1, 2, 3]
					4, 0.3	0.90	
A 2163	0.203	962	2.07	15.36	1, 0.3	13.43	[3, 4]
Perseus	0.018	78	0.15	4.40	3, 0.4	4.80	[3, 5, 6]
					100, 0.3	3.97	
Ophiuchucs	0.028	121	0.41	0.19	5, 0.7	0.19	[3, 4]
					100, 0.3	0.23	

Note. Top two rows correspond to giant radio halos, while the bottom two rows are radio mini-halos. Δd represents the approximate diameter of the RHs. $L_{1.4\text{ GHz, obs}}$ is the total luminosity at 1.4 GHz. M_{200} and R_{200} are taken from Reiprich & Böhringer (2002). We use X-ray-inferred gas densities ρ_{gas} and temperatures for Coma (Briel et al. 1992), for A 2163 and Ophiuchus (Reiprich & Böhringer 2002), and for Perseus (Churazov et al. 2003). For all clusters, we also adopt the outer temperature decrease seen in cosmological cluster simulations (e.g., Pinzke & Pfrommer 2010) and deep *Chandra* X-ray observations (Vikhlinin et al. 2005). Note that despite the fact that Ophiuchus is a CCC with a central temperature dip, we adopt a constant central temperature profile because the dip is only important for radii smaller than 30 h_{70}^{-1} kpc (see Million et al. 2010) and therefore not critical for the surface brightness modeling. The model parameters column indicates the best match values (top row of each cluster) and other acceptable values for the modeling (bottom row of each cluster), and $L_{1.4\text{ GHz, model}}$ is the corresponding predicted total luminosity at 1.4 GHz within R_{200}. See the main text for details. References: [1] Deiss et al. (1997) [2] Briel et al. (1992) [3] Reiprich & Böhringer (2002) [4] Murgia et al. (2009) [5] Pedlar et al. (1990) [6] Churazov et al. (2003).

the magnetic field during the condensation of the cool core (see Aleksić et al. 2010, 2012 for a discussion on the Perseus magnetic field).

The best match to the data is obtained for $\gamma_{\text{tu}} = 3$ and $\alpha_{\text{B}} = 0.4$, however, values as high as $\gamma_{\text{tu}} \approx 100$, and as low as $\gamma_{\text{tu}} = 2$, can be easily accommodated. We recover the surface brightness profile and the total luminosity within 10%. The gamma-ray flux within R_{200} for the $\gamma_{\text{tu}} = 3$ case and for energies above 100 MeV (100 GeV) is $F_\gamma = 1.4 \times 10^{-8}$ (5.1×10^{-12}) cm^{-2} s^{-1}. Adopting $\gamma_{\text{tu}} = 100$ and $\alpha_B = 0.3$, the corresponding gamma-ray flux above 100 MeV (100 GeV) is $F_\gamma = 4.9 \times 10^{-9}$ (1.8×10^{-12}) cm^{-2} s^{-1}. Note that the gamma-ray flux above 100 MeV of the central galaxy NGC 1275 as measured by *Fermi* is 2×10^{-7} cm^{-2} s^{-1} (Abdo et al. 2009), well above our model predictions due to hadronically produced diffuse gamma-ray emission that is expected to glow from the entire cluster.

We can compare these predictions with the upper limit above 1 TeV, and for a region within 0.15 deg around the cluster center, recently obtained by Aleksić et al. (2012). For $\gamma_{\text{tu}} = 3$ $(\gamma_{\text{tu}} = 100)$, we obtain a flux of $F_\gamma(> 1\text{ TeV}, < 0.15\text{ deg}) = 7.3 \times 10^{-14}$ (5.5×10^{-14}) cm^{-2} s^{-1}, which is well below the upper limit of the MAGIC collaboration, $F_{\gamma,\text{UL}}(> 1\text{ TeV}, < 0.15\text{ deg}) \approx 1.4 \times 10^{-13}$ cm^{-2} s^{-1}. Note also that, in the case of $\gamma_{\text{tu}} = 100$, we obtain a maximum CR acceleration efficiency multiplier of $g(\zeta_{\text{p,max}}) = 0.52$, about half of the value adopted by Pinzke & Pfrommer (2010). Note that adopting $g(\zeta_{\text{p,max}}) = 1$ results in slightly smaller gamma-ray luminosities in comparison to those predicted by Pinzke & Pfrommer (2010) and Pinzke et al. (2011) because we additionally account for the central temperature dip and as well as the decrease towards larger radii.

3.1.4. The Ophiuchus radio mini-halo

The Ophiuchus cluster has been widely studied both in radio and X-rays in the last few years because of the claimed presence of a non-thermal hard X-ray tail (Eckert et al. 2008; Fujita et al. 2008; Govoni et al. 2009; Murgia et al. 2009; Pérez-Torres et al. 2009; Nevalainen et al. 2009; Murgia et al. 2010; Million et al. 2010). It was classified as a merging cluster by Watanabe et al. (2001), but more recently Fujita et al. (2008) did not find any evidence of merging and, on the contrary, classified it as one of the hottest clusters with a cool-core (see also Million et al. 2010). The radio mini-halo morphology displays similarities with the thermal X-ray emission. For our modeling we use the surface brightness profile provided by Murgia et al. (2009).

We proceed as before, adopting a central magnetic field value of $B_0 = 10\,\mu$G. The best match to the data is obtained for $\gamma_{\text{tu}} = 5$ and $\alpha_B = 0.7$. However, values as high as $\gamma_{\text{tu}} \approx 100$, and as low as $\gamma_{\text{tu}} = 2$, can be easily accommodated. We recover the surface brightness profile and the total luminosity within 20%. The gamma-ray flux within R_{200} for the $\gamma_{\text{tu}} = 5$ case and for energies above 100 MeV (100 GeV) is $F_\gamma = 1.2 \times 10^{-10}$ (4.3×10^{-14}) cm^{-2} s^{-1}. Adopting $\gamma_{\text{tu}} = 100$ and $\alpha_B = 0.3$, the corresponding gamma-ray flux above 100 MeV (100 GeV) is $F_\gamma = 8.3 \times 10^{-11}$ (3.1×10^{-14}) cm^{-2} s^{-1}. The gamma-ray flux is, in both cases, about two orders of magnitude lower than the upper limit obtained by *Fermi*-LAT (Ackermann et al. 2010a). Note also that in the case of $\gamma_{\text{tu}} = 100$ we obtain a maximum CR acceleration efficiency multiplier of $g(\zeta_{\text{p,max}}) = 0.014$.

3.2. Discussion and conclusions on the hybrid hadronic model

After these detailed considerations on four individual RHs, we are now summarizing the main points:

1. The radio mini-halos in Perseus and Ophiuchus can be easily reproduced in our hybrid hadronic model with a wide range of possible values for γ_{tu}. In contrast, the large extension of the giant radio halos in Coma and Abell 2163 in comparison to the X-ray emission requires lower values of $\gamma_{\text{tu}} \lesssim 4$ in order to match the data. However, we would expect higher values for γ_{tu} in merging NCCCs that are highly turbulent (Enßlin et al. 2011). There are four possibilities that can explain this apparent contradiction. (i) Primary electrons accel-

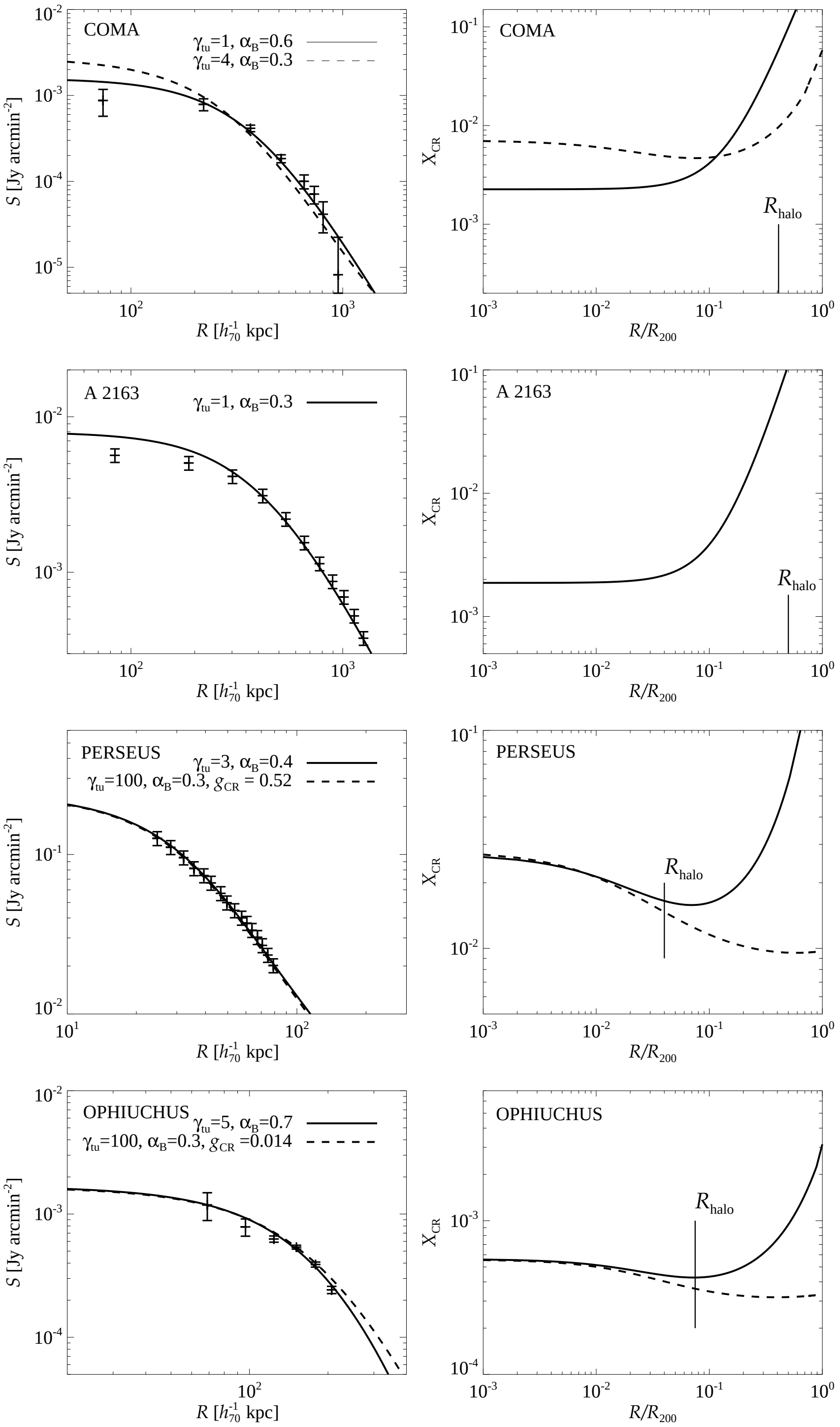

Fig. 5. Surface brightness modeling of the RHs in Coma, Abell 2163, Perseus and Ophiuchus. The left panels show the RHs' azimuthally averaged surface brightness profiles, while the right panels show the corresponding CR-to-thermal pressure profiles $X_{CR}(r)$ where we additionally mark the RHs' radial extension by a vertical bar. Note that different parameter values that yield almost the same surface brightness profile, result in very different X_{CR} profiles. In the case of Abell 2163 and Ophiuchus, we adopt a 10% uncertainty range instead of the errors reported by Murgia et al. (2009) to account for additional systematic uncertainties, e.g., residual point source contamination. We also adopt a 10% uncertainty range for Perseus, for which Pedlar et al. (1990) do not report any uncertainty intervals.

erated in outer shocks, which we do not consider here, could have an important contribution to the RH emission, particularly in the cluster outskirts (Pfrommer et al. 2008). While this does not have to significantly enhance the total luminosity, it could account for the larger radial extent of the radio surface brightness in comparison to the thermal X-ray emission. (ii) Merging clusters are not spherically symmetric as can be seen in Coma and Abell 2163, requiring inherently non-spherical modelling. In order to reproduce the more extended radio emission relative to the thermal X-ray emission, the non-thermal clumping factor, $C_{\mathrm{non-th}}$, needs to be larger than its thermal analogue, C_{th}, in concentric spherical shells, where we defined those statistics by

$$C_{\mathrm{non-th}} = \left\langle \rho_{\mathrm{gas}} C \right\rangle / \left\langle \sqrt{\rho_{\mathrm{gas}} C} \right\rangle^2 , \qquad (15)$$

$$C_{\mathrm{th}} = \left\langle \rho_{\mathrm{gas}}^2 \right\rangle / \left\langle \rho_{\mathrm{gas}} \right\rangle^2 . \qquad (16)$$

This appears to be the case since the radio surface brightness emission is more elongated than its counterpart in thermal X-rays and needs to be carefully quantified in future work. (iii) CR streaming and diffusive transport may cause a possible spectral steepening in the cluster core region that would imply spatial variations of the CR spectral index throughout the cluster and hence a spatially varying radio emission, in particular in the cluster outskirts. (iv) Adopting the simulation-derived $\tilde{C}$ profile (Pinzke & Pfrommer 2010) for our hybrid model may have biased the inner slope of the CR density profile to become too steep due to the overcooling problem of purely radiative simulations. This produces cluster cores that are too dense (in comparison to observations), which also should overestimate the rate of adiabatic compression that is experienced by the CR population during the formation of the cooling core. Hence, the resulting values of γ_{tu} are then biased low in comparison to a potentially shallower slope of the inner CR profile. To quantify the last point, we try to reproduce the Coma surface brightness using a model without $\tilde{C}$. We find that values as high as $\gamma_{\mathrm{tu}} \approx 8$ can be accommodated. However, $\gamma_{\mathrm{tu}} = 1$ still represents the best match to the data, demonstrating that the problem can be weakened but not circumvented even in this case of a cored CR profile. Nevertheless, we can successfully reproduce the morphology of Coma and Abell 2163 RHs, solving the previous problems of the *classical* hadronic model (see, e.g., Donnert et al. 2010a).

2. Gamma-ray and radio emission are complementary tools in constraining the CR population. While gamma-ray emission is a direct way to constrain the CR pressure, it is also critical in disentangling between the hadronic and re-acceleration model. In contrast, the information derived from the radio window is degenerate with the assumptions on the magnetic field strengths. Nevertheless, we find that RH measurements allow tighter constraints on the CR pressure (except for the case of Coma).
3. The magnetic field values adopted here are perfectly in agreement with other observational constraints, solving previous tensions of the *classical* hadronic model (see, e.g., Jeltema & Profumo 2011). Indeed, different values of B_0 could be adopted without violating other observational constraints. The exception to this is again Coma, for which a higher B_0 value would be in contradiction with Faraday rotation measure data (Bonafede et al. 2010), leaving room for central magnetic field strengths around 1–5 μG that are in agreement with the data (Arlen et al. 2012). Only a value much lower would imply a level of the gamma-ray emission that challenges the most recent *Fermi* limit (Zimmer et al. 2012).
4. Considering the case of advection-dominated CR transport ($\gamma_{\mathrm{tu}} \gtrsim 100$), which only allows for a good match to the data of Perseus and Ophiuchus, the g_{CR} parameter can be interpreted as the maximum CR acceleration efficiency used in Pinzke & Pfrommer (2010). If the cluster CR population is mainly accelerated in cosmological structure formation shocks, then this value should depend on the mass accretion history and should be approximately universal, i.e., similar for all clusters. We find $g_{\mathrm{CR,Perseus}} = 0.52$ and $g_{\mathrm{CR,Ophiuchus}} = 0.014$, because we fixed $B_0 = 10\ \mu$G in both cases and used g_{CR} as normalization. This discrepancy can be resolved by increasing/lowering the central magnetic field in Perseus/Ophiuchus to $B_{0,\mathrm{Perseus}} \approx 20\ \mu$G and $B_{0,\mathrm{Ophiuchus}} \approx 1\ \mu$G. We note, however, that without the guidance of cosmological cluster simulations that include CR streaming, the data does not yet constrain γ_{tu}.
5. The small cluster sample analysed here was only meant to serve as a proof of concept and to demonstrate the viability of matching observed RH data with our hybrid hadronic model. This is in especially true because of the comparably large parameter space that the physics modeled here demands and which encompasses our parametrization of the magnetic field (B_0, α_B), γ_{tu}, and the CR acceleration efficiency function. Particularly, a large region of the (γ_{tu}, α_{B}) parameter space is available for the analyzed radio mini-halos (note also that the parameters γ_{tu} and α_{B} are degenerate). Future work on all known RHs may provide better insight, but is beyond the scope of this work.

Summarizing, we find that the hybrid hadronic model that includes microscopic CR transport successfully reproduces the main morphological characteristics of both giant and mini-halos without violating gamma-ray constraints. As we will see in the next section, it can also reproduce the radio-to-X-ray scaling relation, solving the previous problems of the *classical* hadronic model, and the radio-to-SZ scaling relation.

4. Radio Scaling Relations

As introduced in Section 1, there exist an apparent bimodality between the radio and X-ray cluster emission. Clusters with a given X-ray luminosity can either host RHs or show an absence of diffuse radio emission (see, e.g., Brunetti et al. 2009; Enßlin et al. 2011). More recently, a study of the radio-to-SZ scaling relation revealed the absence of a strong bimodality dividing the cluster population into radio-loud and radio-quiet clusters (Basu 2012). Since Y_{SZ} correlates more tightly with cluster mass than L_{X}, this may indicate that the larger scatter of L_{X} correlates with the scatter of the radio luminosity in such a way that it produces a bimodality; but as a result of a second (hidden parameter) rather than the fundamental cluster parameter – its mass. In this section, we investigate these two scaling relations in the framework of our extended hadronic scenario.

4.1. Exploring the parameter space of scaling relations

In Figure 6, we show the general scaling relations of our hybrid CR model of Section 2.5 applied to the MultiDark sample. We show how both the radio-to-X-ray and the radio-to-SZ scaling relations differ upon varying the parameters γ_{tu}, B_0, α_{B} and redshift. We fix the CR-normalization parameter g_{CR} to 0.5 in all cases, ensuring an average CR-to-thermal pressure of 2%

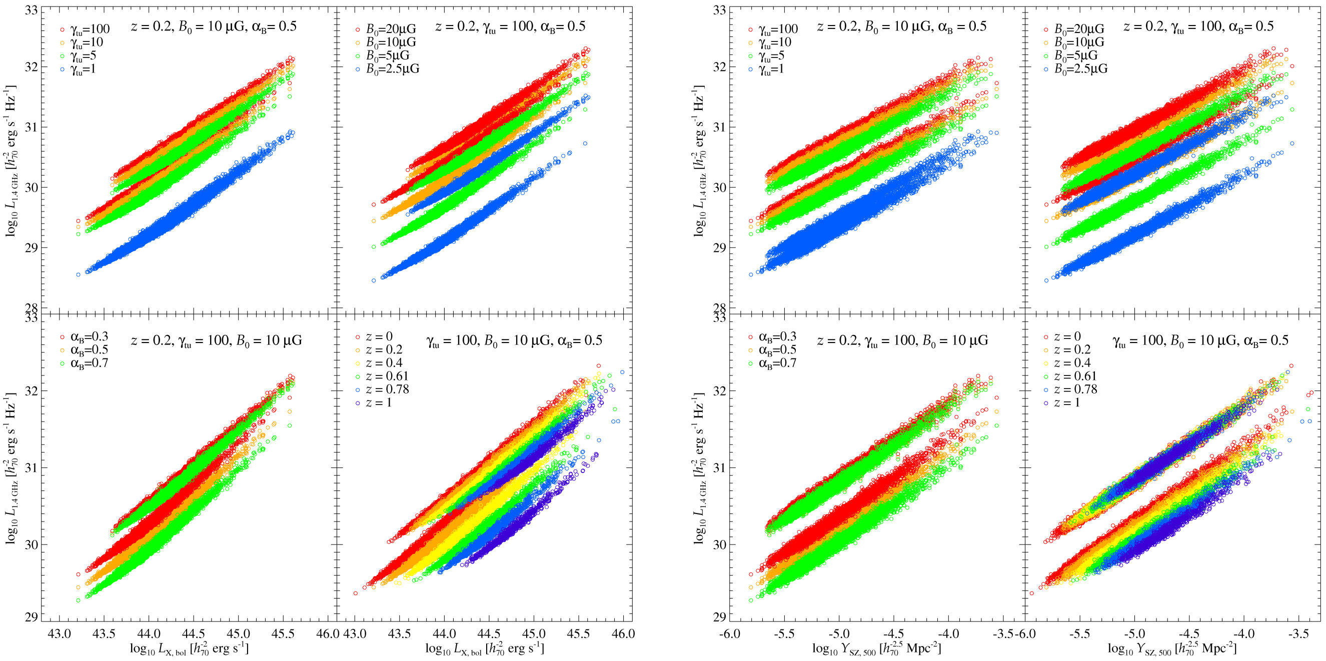

Fig. 6. Radio-to-X-ray and radio-to-SZ scaling relations as predicted by our hybrid CR model. In the left panel, we show how the $L_{1.4\ \mathrm{GHz}} - L_{\mathrm{X,bol}}$ relation varies upon changing different parameters. In the right panel, we show the same, but for the $L_{1.4\ \mathrm{GHz}} - Y_{\mathrm{SZ},500}$ relation. Note that in each plot there are two separated populations for each model realization, shown with the same color. The upper sets of points correspond to the CCC population while the lower sets correspond to NCCCs. The plot labels indicate those parameters which are kept fixed. We fix the g_{CR}-normalization parameter to 0.5 for all cases. See main text for details.

(0.05%) within R_{500} ($R_{500}/2$). Here, the radio luminosity is calculated at 1.4 GHz within R_{500}.[10] In our CR model, we fix the CR number for $\gamma_{\mathrm{tu}} = 100$ using Equation (36) of Enßlin et al. (2011), integrating up to R_{500}. To compute the radio luminosity for different values of γ_{tu}, we employ CR number conservation (for CR energies $E >$ GeV where Coulomb cooling is negligible for CR protons).

In each panel in Figure 6 there are two separated populations for each model realization (i.e., for a given set of parameters). Each upper set of points corresponds to the CCC population while the lower set corresponds to NCCCs, respectively. In our model, the radio and X-ray emissivities scale with the square of the gas density so that $L_{1.4\ \mathrm{GHz}}$ and $L_{\mathrm{X,bol}}$ are significantly higher for CCCs in comparison to NCCCs. In contrast, Y_{SZ} only depends weakly on the central gas density as explained in Section 2.3. This explains the relative location of the NCCC and CCC populations in the $L_{1.4\ \mathrm{GHz}} - L_{\mathrm{X,bol}}$ and $L_{1.4\ \mathrm{GHz}} - Y_{\mathrm{SZ}}$ planes. In particular, CCCs are shifted to the upper right in the $L_{1.4\ \mathrm{GHz}} - L_{\mathrm{X,bol}}$ plane while they are shifted vertically upward in the plane spanned by $L_{1.4\ \mathrm{GHz}} - Y_{\mathrm{SZ}}$. In reality, we expect an (ab initio unknown) distribution of these parameters which would substantially increase the scatter in the scaling relations and possibly lead to a bimodality, depending on correlations among the different parameters.

Most interestingly, the slope of the radio scaling relations does not differ when varying parameter values because we do not include any cluster mass-dependence in our parametrizations which is neither required nor constrained by current data. Closely inspecting Figure 6, we see that we obtain the largest changes in $L_{1.4\ \mathrm{GHz}}$ for variations in $1 < \gamma_{\mathrm{tu}} < 5$ and B_0 over the parameter range probed, albeit with a stronger dependence for weaker field strengths (as expected from Equation 5).

4.2. Comparison to observations

After collecting the X-ray luminosity and the SZ flux of known RHs, we compare the resulting scaling relations to a phenomenological model realization that was chosen to additionally obey other observational constraints (e.g., from Faraday rotation studies) as well as theoretical considerations on CR transport.

4.2.1. Observational samples

In Appendix D we construct a sample of giant radio halos (black) and radio mini-halos (red), as well as upper limits on the radio emission (Brunetti et al. 2009; Enßlin et al. 2011; Govoni et al. 2009), and show this in the left panel of Figure 7. The median redshift of this sample is $z \approx 0.18$. The corresponding observational scaling relation is well fit by $\log_{10} L_{1.4\ \mathrm{GHz}} = A + B \log_{10} L_{\mathrm{X,bol}}$ with $A = -37.204 \pm 1.838$ and $B = 1.512 \pm 0.041$, and a scatter of $\sigma_{yx} \approx 0.52$ (we do not include upper limits in the fit; units are as in Figure 7). We refer the reader to Brunetti et al. (2009) and Enßlin et al. (2011) for an extensive discussion on this topic. We emphasize that in contrast to giant radio halos, mini-halos span a wider range in radio luminosity (as also pointed out by Murgia et al. 2009). The Perseus mini-halo (highest radio mini-halo luminosity in the left panel of Figure 7), e.g., has a radio luminosity that is almost an order of magnitude higher than in giant radio halos at the same X-ray luminosity. In contrast, the Ophiuchus mini-halo (lowest radio mini-halo luminosity in the left panel of Figure 7), which is representative of a few other similar examples recently detected in CCCs (such as A2029 and A1835), has a radio luminosity which

---

[10] The mean (median) difference between calculating L_ν within R_{200} or R_{500} is 5.3% (5.6%).

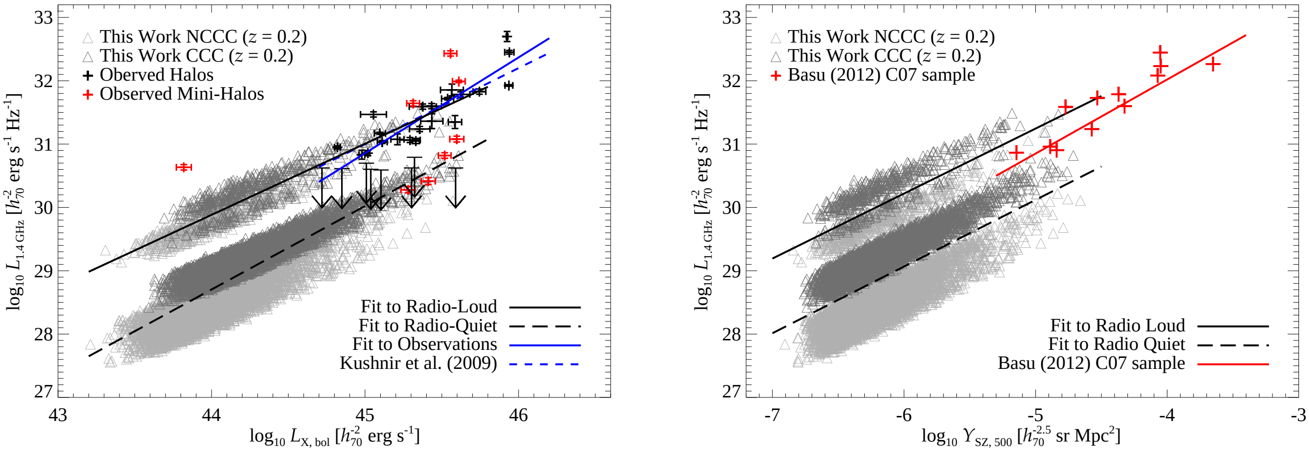

Fig. 7. Radio-to-X-ray and radio-to-SZ scaling relations in our hybrid CR model (see main text for the details of the chosen parameters) compared with observations. *Left.* $L_{1.4\,\mathrm{GHz}} - L_{\mathrm{X,bol}}$ relation in comparison to the observational sample taken from the literature and detailed in Appendix D. *Right.* $L_{1.4\,\mathrm{GHz}} - Y_{\mathrm{SZ}}$ relation in comparison to the observational sample C07 from Basu (2012).

is much lower than giant radio halos in merging clusters and is even below the upper limits.

We caution that the determination of the slope of the observational $L_{1.4} - L_{\mathrm{X,bol}}$ relation is not very robust because of the small sample size of RHs, selection biases of extended low-surface brightness objects, and systematic uncertainties in the measurements of $L_{1.4}$ and $L_{\mathrm{X,bol}}$. The recently detected low-luminosity mini-halos exemplify those uncertainties and the large intrinsic scatter of this relation. On the other hand, X-ray luminosities for the same object as derived by, e.g., *ROSAT* and *Chandra* can easily differ by a factor of a few.[11] In the left panel of Figure 7, we additionally show the model of Kushnir et al. (2009) with a slope of ≈ 1.2, arbitrarily normalized for visual purposes, from their simple analytical hadronic model.

In order to compare our model to the observed 1.4 GHz radio-to-SZ scaling relation, we use the result by Basu (2012) that is based on the radio halo sample from Cassano et al. (2007) (hereafter C07), which has a median redshift of $z \approx 0.18$ and excludes radio mini-halos. For this sample, Basu (2012) computes Y_{SZ} within the radio-halo radii given by Cassano et al. (2007). These radii have a median of about 0.5 h_{70}^{-1} Mpc which compares favourably with the median of $R_{500} \approx 0.4\ h_{70}^{-1}$ Mpc in our MultiDark $z = 0.2$ snapshot. For the C07 sample, Basu (2012) obtains a scaling relation in the form of $\log_{10} L_{1.4\,\mathrm{GHz}} = A + B\ \log_{10} Y_{\mathrm{SZ}}$ with $A = 29.7 \pm 0.8$ and $B = 1.17 \pm 0.18$, and a scatter of $\sigma_{yx} \approx 0.28$ (units are as in Figure 7). The same comments regarding the small sample size of RHs, selection biases, and systematic uncertainties in the luminosity measurements also apply here.

4.2.2. Model realization

In order to compare our model prediction with observations, we select a particular realization of our model. To this end, we use the MultiDark cluster sample at $z = 0.2$, which compares well with the redshift of the observational samples; see above and Appendix D. We divide our cluster sample randomly into radio-quiet and radio-loud clusters, assuming a ratio of 10% of the latter. We use the turbulent propagation parameter γ_{tu} to separate both populations. In radio-quiet clusters, we assign $\gamma_{\mathrm{tu}} = 1$, and in radio-loud clusters, we adopt randomly and uniformly γ_{tu} values in the intervals $[40, 80]$ and $[1, 5]$ for NCCCs and CCCs, respectively. We note that those values for γ_{tu} would produce slightly too concentrated surface brightness profiles for giant radio halos. As laid out in detail in Section 3.2, this may be an artifact caused by a combination of four effects, namely additional primary radio emission in the cluster periphery, an enhanced non-thermal clumping factor, spatial variations of the CR spectral index, and our choice of simulation-derived CR profiles that may be too concentrated as a result of the overcooling in radiative simulations without AGN feedback. Moreover, we demonstrate in Figure 6 that the normalization of the RH luminosity is highly degenerate with our other parameters so that a different combination of those could mimic a similar normalization for smaller values of γ_{tu}.

Our modeling of magnetic fields is inspired by Faraday rotation studies that point to higher field values in the core region of CCCs compared to NCCCs (Kuchar & Enßlin 2011; Bonafede et al. 2010), presumably due to the higher adiabatic compression factor during the formation of the cooling core. Hence, for radio-quiet clusters, we adopt randomly and uniformly distributed values of the central magnetic field B_0 in the intervals $[2.5, 5.5]\ \mu$G and $[5, 10]\ \mu$G for NCCCs and CCCs, respectively. To account for the potential turbulent dynamo in radio-loud objects (characterized by a higher turbulent transport parameter in our model), we slightly increase B_0 in those objects and chose B_0 intervals of $[4.5, 7.5]\ \mu$G and $[7.5, 12.5]\ \mu$G for NCCCs and CCCs, respectively.

We fix $\alpha_{\mathrm{B}} = 0.5$ and $g_{\mathrm{CR}} = 0.5$ for all clusters. We note that our parameter choices are mostly phenomenologically driven with the aim to reproduce observations. The parameter study in Figure 6 exemplifies considerable degeneracies so that different combinations of parameters can potentially result in very similar distributions. We emphasize the need of more detailed observations of radio halos and in particular of multi-frequency correlation studies to constrain the interplay of some of these parameters.

---

[11] For example, the bolometric X-ray luminosity of A 2163 as measured by *ROSAT* is $8.65 \times 10^{45}\ h_{70}^{-1}$ erg s^{-1} (Brunetti et al. 2009) while the *Chandra* measurement is $4.93 \times 10^{45}\ h_{70}^{-1}$ erg s^{-1} (Cavagnolo et al. 2009; ACCEPT: Archive of Chandra Cluster Entropy Profile Tables; http://www.pa.msu.edu/astro/MC2/accept/).

In Figure 7, we show our model in comparison to the observed radio-to-X-ray and radio-to-SZ scaling relations. The normalization of our model can be arbitrarily varied by changing g_{CR} as long as the resulting X_{CR} respects the current observational constraints (see, e.g., Aleksić et al. 2012) and remains below a few percents. As explained above, our choice of $g_{CR} = 0.5$ ensures an average CR-to-thermal pressure of 2% within R_{500}, allowing for plenty of available parameter space to match the observational constraints. Our model is sufficiently flexible to either mimic a cluster radio bimodality or not, depending on the parameters adopted for the populations of radio-loud and radio-quiet objects.

However, with the given model realization as in Figure 7, the separation of the radio-loud and radio-quiet populations is substantially larger in the $L_{1.4\ \mathrm{GHz}} - L_{\mathrm{X,bol}}$ plane than in the $L_{1.4\ \mathrm{GHz}} - Y_{\mathrm{SZ}}$ plane, which exhibits almost a continuum distribution from radio-loud CCCs to the radio-quiet NCCCs. This is mainly because the bolometric X-ray emissivity scales with ρ_{gas}^2 while $Y_{\mathrm{SZ}} \propto \rho_{\mathrm{gas}}$ (which is only strictly valid for an isothermal gas distribution). As a consequence, the highly peaked gas profiles of CCCs have less impact on Y_{SZ} than on $L_{\mathrm{X,bol}}$. This is one plausible explanation for the observed discrepancy of the presence of a bimodality in $L_{1.4\ \mathrm{GHz}} - L_{\mathrm{X,bol}}$ and the apparent absence of it in $L_{1.4\ \mathrm{GHz}} - Y_{\mathrm{SZ}}$.

The slope of our model depends on the different parameter choices and, particularly, on the relative differences introduced for the NCCC/CCC and the radio-loud/quiet populations. However, we note that our $L_{1.4\ \mathrm{GHz}} - L_{\mathrm{X,bol}}$ is slightly shallower than the observed relation, more similar to the Kushnir et al. (2009) prediction, and that the slope of our $L_{1.4\ \mathrm{GHz}} - Y_{\mathrm{SZ}}$ compares well with the observed slope. Owing to the many uncertainties and lack of robustness both in the observations and modeling at this stage, we do not attempt to fine-tune our model to the observations.

5. Radio Luminosity Function

5.1. Comparison with observations at 1.4 GHz

In Figure 8, we show the RH luminosity function (RLF) at 1.4 GHz for a representative realization of our hybrid CR model (as in Section 4), and compare it with observational results. As for the XLF, the RLF is completely determined by the cluster mass function and the radio luminosity-to-mass relation, through $L_{1.4\ \mathrm{GHz}} - L_{\mathrm{X,bol}}$ or $L_{1.4\ \mathrm{GHz}} - Y_{\mathrm{SZ}}$ in combination with our phenomenological gas model. However, in the radio band there is the additional uncertainty of the fraction of radio-loud clusters. Thus, in Figure 8, we also show the RLFs obtained by applying the $L_{1.4\ \mathrm{GHz}} - L_{\mathrm{X,bol}}$ and $L_{1.4\ \mathrm{GHz}} - Y_{\mathrm{SZ}}$ relations to simulated clusters of the MultiDark snapshot at $z = 0.2$, using our phenomenological gas model for $L_{\mathrm{X,bol}}$ and $Y_{\mathrm{SZ,500}}$ of each cluster, respectively. Note that this procedure is *only* applied to halos defined as radio-loud clusters (which are by definition accounted for in the $L_{1.4\ \mathrm{GHz}}$ scaling relations) and we assume a fraction of 100%, 25%, 10%, 5% and 1% of radio-loud clusters. As evident from Figure 8, this is different from our model for the radio luminosity, where we also define a fraction of radio-loud clusters. However, the radio-quiet population also contributes to the RLF with an increasing fraction at low luminosities. This is exemplified in the top left plot of Figure 8, which shows the contribution of radio-quiet and loud populations to the total RLF, assuming a fraction of 25% and 1% of radio-loud objects.

In Appendix D, we make an attempt to construct an RLF from existing X-ray flux-limited radio surveys. There exist two such studies, the cluster radio survey done with the National Radio Astronomy Observatory (NRAO) Very Large Array (VLA) sky survey (NVSS) at 1.4 GHz of Giovannini et al. (1999) and the survey with the Giant Metrewave Radio Telescope (GMRT) at 610 MHz by Venturi et al. (2007, 2008). For the latter, one can also construct an RLF at 1.4 GHz using the corresponding RH follow-up measurements. The fractions of radio-loud clusters are about 6%, 18% and 24% for the NVSS 1.4 GHz, GMRT 610 MHz and GMRT 1.4 GHz samples, respectively. As explained in Appendix D, we use the 1.4 GHz NVSS RLF (with a median redshift of $z \approx 0.18$) as observational reference for our comparisons. We conclude that the observational determinations of the RLF is not very robust at this stage; the very different fractions of radio-loud clusters found in the different studies is one indicator of this.

Generally, there is fair agreement between the NVSS RLF and both our modeled RLF and the RLFs based on observational scaling relations, particularly for radio-loud fractions between 10% and 1%. In particular, we verified that the cumulative number of RHs above a certain flux limit of the NVSS survey is well matched by our 10%-loud fraction case, which will be used in the following section. The RLF obtained from the $L_{1.4\ \mathrm{GHz}} - L_{\mathrm{X,bol}}$ relation differs from the NVSS RLF at high luminosities, presumably caused by the large observed scatter. On the other side, the RLF obtained from the $L_{1.4\ \mathrm{GHz}} - Y_{\mathrm{SZ}}$ relation matches the NVSS result better. These results need to be consolidated by RLFs corrected for flux-incompleteness and simulations of larger cosmological volumes that are more complete at the high-mass end. Figure 8 shows that it will be difficult to discriminate between different scenarios at high radio luminosities (or equivalently masses). Indeed, in the bottom right panel of Figure 8 we compare our RLF and the RLFs based on observational scaling relations for a 10% fraction of radio-loud clusters to the NVSS RLF. This suggests that the low-luminosity (low-mass) clusters will be the most useful in disentangling between different models. This emphasizes the importance of conducting homogeneous, well controlled surveys of radio halos with the extended VLA at 1.4 GHz and LOFAR at lower frequencies. Since the latter has already started to take data, it is extremely timely to present RLF predictions for this wavelength regime in our model, which we will do next.

5.2. Low-frequency predictions at 120 MHz

In Figure 9, we show our model predictions at 120 MHz obtained with the same representative realization of our model as in Section 4, with 10% radio-loud clusters. We show both the differential RLF (top left panel) and the cumulative number density (bottom left panel) at different redshifts (corresponding to different MultiDark snapshots of Table 1). We note that our imposed mass cutoff of $M_{200} = 10^{14}\,h^{-1}\,M_{\odot}$, which has been adopted to reliably model the cluster gas distribution, translates into a luminosity cutoff. This causes the differential luminosity function to turn over at the low-luminosity end and may artificially flatten the slope already at sightly higher luminosities than the luminosity maximum that indicates our formal incompleteness limit.

Additionally shown in Figure 9 is the expected LOFAR Tier 1 *point-source* flux limit of $F_{5\sigma}^{\mathrm{PS}} = 0.5$ mJy (Röttgering et al. 2012) converted to a luminosity limit at a few representative redshifts. This flux limit is clearly an underestimate for nearby RHs, which extend over angular scales ~ 1 deg, as e.g., in the case of the Coma radio halo. In order to make more reliable predictions, in the following, we will calculate the RH flux limit with Equation (10) of Cassano et al. (2010), approximating the halo

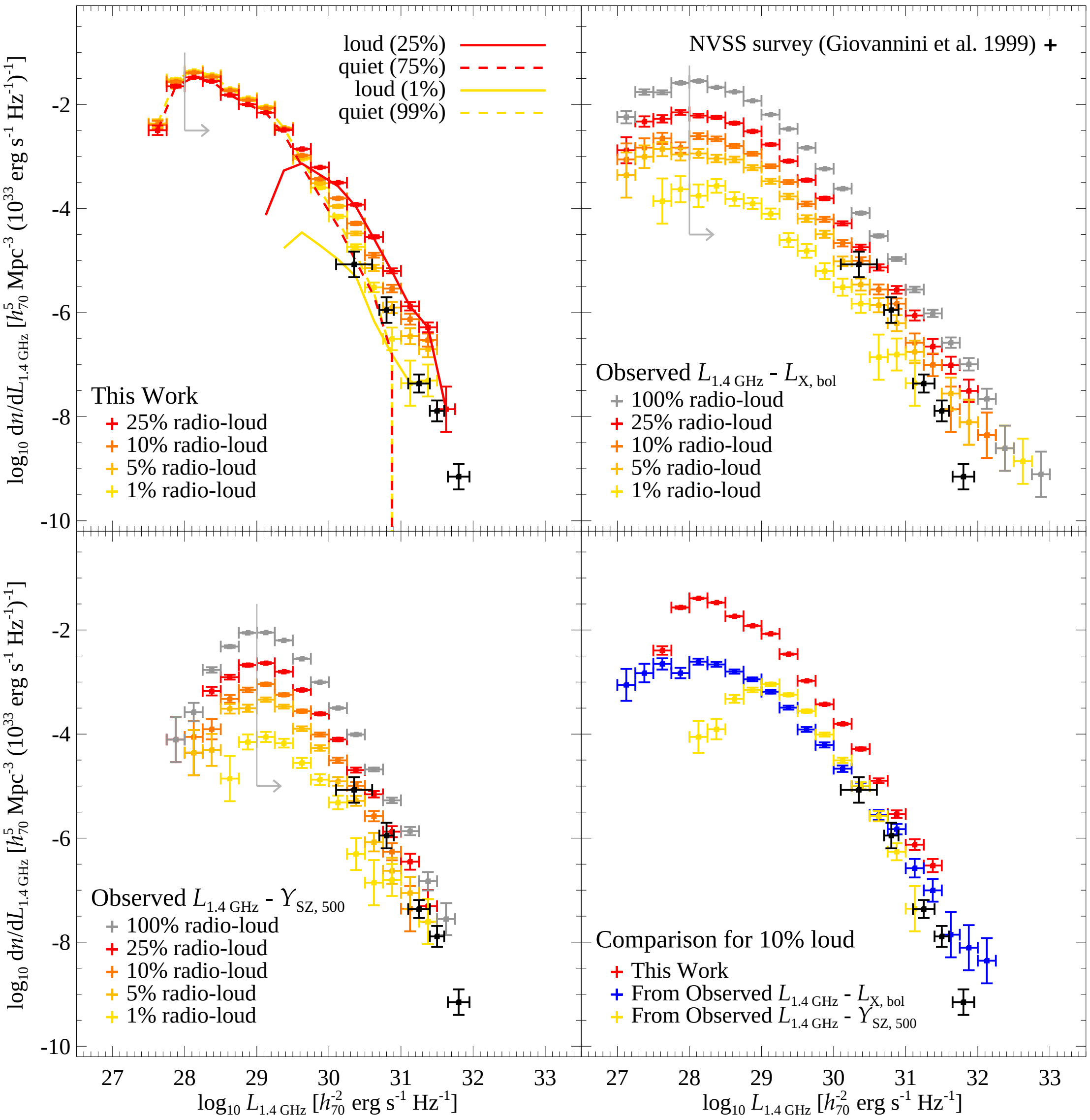

Fig. 8. RH luminosity function (RLF) at 1.4 GHz. The top left panel shows the RLF of our hybrid CR model (see main text for the details of the chosen parameters) for different fractions of radio-loud clusters. Additionally shown is the contribution of radio-quiet and radio-loud populations to the total RLF (assuming a fraction of 25% and 1% of radio-loud objects). The top right panel shows the RLF obtained by applying the observed $L_{1.4\,\mathrm{GHz}} - L_{\mathrm{X,bol}}$ relation to the MultiDark clusters at $z = 0.2$, using our phenomenological gas model for $L_{\mathrm{X,bol}}$ of each cluster; again for different percentages of radio-loud clusters. The bottom left panel shows the RLF obtained by applying the observed $L_{1.4\,\mathrm{GHz}} - Y_{\mathrm{SZ,500}}$ relation to the MultiDark clusters at $z = 0.2$, using $Y_{\mathrm{SZ,500}}$ of our our phenomenological gas model for each cluster. The bottom right panel shows the comparison between the three approaches for 10% of radio-loud clusters. In all panels, we show the NVSS survey RLF (Giovannini et al. 1999) with a median redshift of $z \approx 0.18$, corrected for the sample incompleteness and survey sky coverage. Horizontal error bars represent the mass bins while the vertical error bars are Poissonian uncertainties. The light gray line marked by the arrow estimates the incompleteness limit owing to the adopted low-mass cut (see Section 2) and the scatter in the halo luminosities.

extension by R_{500} and requiring the mean flux within the RH half-radius to be higher than $F_{5\sigma}^{\mathrm{PS}}$. This may result in an overestimation of the flux limit for CCCs, whose radio emission is more centrally concentrated than in NCCCs. The median R_{500} of our sample is about 0.4 h_{70}^{-1} Mpc at all redshifts. This translates to a flux limit of about 30 mJy at $z = 0.1$, 7 mJy at $z = 0.2$ and 0.5 mJy (equal to the point-source value) at $z \approx 0.6$.

To derive low-frequency flux functions, we construct an analytical model for the evolving RLF. We fit the 120 MHz RLF at different redshifts with a second-order polynomial of the form $\log_{10} \mathrm{d}n/\mathrm{d}L_{120\,\mathrm{MHz}} = A_0 + A_1 \log_{10} L_{120\,\mathrm{MHz}} + A_2 (\log_{10} L_{120\,\mathrm{MHz}})^2$. All luminosities are measured in units of h_{70}^{-2}erg s^{-1} Hz^{-1} and (comoving) number densities in units of h_{70}^3 Mpc^{-3}. We consider only luminosities with $\log_{10} L_{120\,\mathrm{MHz}} \geq 29.25$ to exclude the turn-over at low luminosities caused by incompleteness. To obtain an analytical model for $n(L, z)$, we constrain the evolution of the three free parameters A_i to follow a

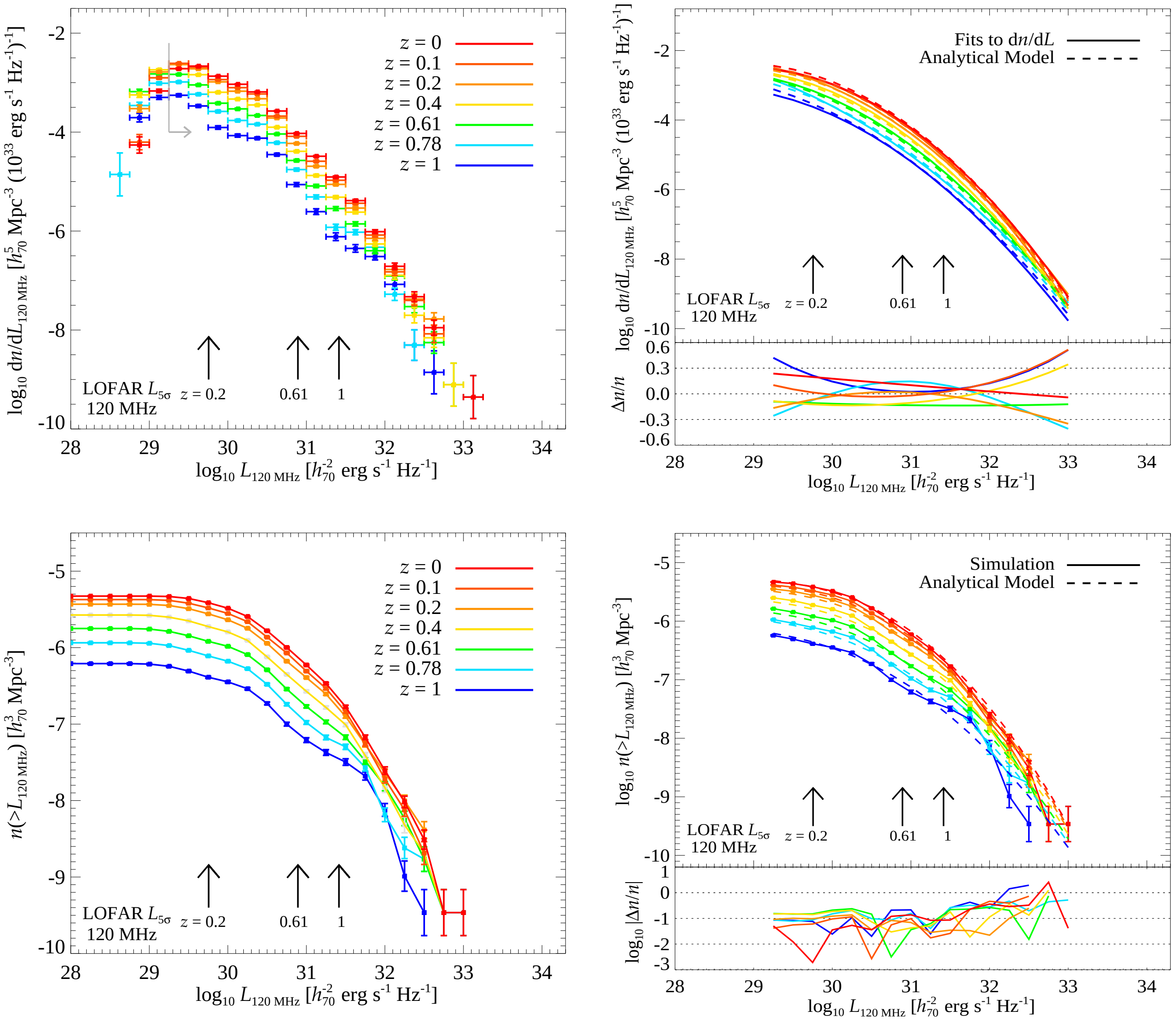

Fig. 9. RH luminosity function $n(L, z)$ at 120 MHz (top left panel) and cumulative number density of RHs $n(> L, z)$ (bottom left panel) at different redshifts z (color coded) for the model realization described in Section 4 with a 10% fraction of radio-loud clusters. To obtain an analytical model for $n(L, z)$, we fit the logarithm of the RLF at each z with a second-order polynomial and constrain the evolution of the three free parameters to follow a linear function in $1 + z$ (see main text for details). The right panels show the comparison of the RLF fits (top) and the cumulative number density of the MultiDark samples (bottom) to the constrained analytical model. The bottom panels of these two panels show the relative differences $\Delta n/n = (n_{\mathrm{analytical}} - n_{\mathrm{fit}})/n_{\mathrm{fit}}$. Additionally shown is the LOFAR Tier 1 *point-source* flux limit of $F^{\mathrm{PS}}_{5\sigma} = 0.5$ mJy (Röttgering et al. 2012) converted to a luminosity limit at a given redshift. Horizontal error bars represent the mass bins while the vertical error bars are Poissonian uncertainties. The light gray line marked by the arrow estimates the incompleteness limit owing to the adopted low-mass cut (see Section 2) and the scatter in the halo luminosities.

linear function in $1 + z$, i.e., $A_i = A_{i,0} + A_{i,1}\ (1 + z)$.[12] In the right panels of Figure 9, we compare the RLF fits (top) and the cumulative number density in the simulation (bottom) to the analytical model. In particular the analytics matches the simulation well except for high luminosities and high redshifts where small number statistics explains the deviations.

This analytical model describes the number of RHs expected in our model per unit luminosity and per unit comoving volume V_c, i.e., $\mathrm{d}^2N(L, z)/\mathrm{d}V_c\mathrm{d}L$. Hence the cumulative number of RHs above a given flux limit F is given by the integral

$$N(> F) = \int_{z_1}^{z_2} \int_{L(F)}^{\infty} \frac{\mathrm{d}^2N(L, z)}{\mathrm{d}V_c\mathrm{d}L} \frac{\mathrm{d}V_c}{\mathrm{d}z}\, \mathrm{d}z\, \mathrm{d}L, \qquad (17)$$

where $L(F) = 4\pi D(z)^2 F$ and $D(z)$ is the luminosity distance to an RH at redshift z. The result is shown in the left panel of Figure 10 for the model realization described in Section 4 with a 10% fraction of radio-loud clusters (black solid line). We limit the integral to luminosities $\log_{10} L_{120\,\mathrm{MHz}} \geq 29.25$. Our redshift integration extends from $z_1 = 0.018$, the redshift of the closest known RH in Perseus, to $z_2 = 2$. As shown in Figure 10, already

---

[12] The values of these parameters are $A_{0,0} = -436.79$, $A_{0,1} = 109.75$, $A_{1,0} = 29.68$, $A_{1,1} = -7.17$, $A_{2,0} = -0.51$ and $A_{2,1} = 0.12$.

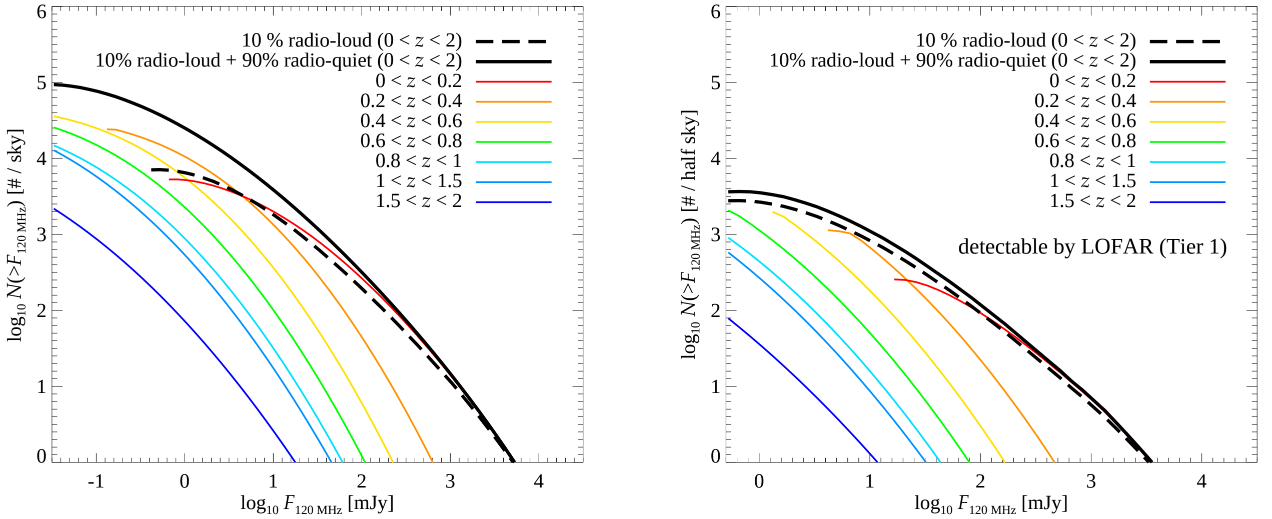

Fig. 10. Cumulative number of RHs above a certain flux limit in an all-sky survey at 120 MHz. We show the result of the model realization described in Section 4 using all clusters and adopting a fraction of 10% of radio-loud clusters (black solid line). Additionally, we show the result obtained by using the 10% radio-loud clusters *only* (black dashed line). We also show the differential contribution to the RLF in redshift slices. Note that the number of (detectable) RHs would be dramatically reduced by the presence of a break in the model at some low luminosity-scale, or a mass-dependence of the model parameters causing the RH luminosities to decrease at low masses. *Left.* Total number of RHs in the sky. *Right.* Number of detectable RHs by the LOFAR Tier 1 survey considering its sky coverage (half sky) and adopting a realistic flux limit corresponding to different angular source extensions at different redshifts. The point-source flux limit, which applies to distant clusters with $z \gtrsim 0.6$, is taken to be $F_{5\sigma}^{\mathrm{PS}} = 0.5$ mJy (see main text for details).

redshifts $z \gtrsim 1$ do not significantly contribute to the flux function. Additionally, there are large theoretical uncertainties since our gas model is not calibrated for these redshifts (and implied low-mass range) and very little is observationally known about diffuse radio emission on group scales in particularly at these redshifts, which motivates our upper redshift limit.

Figure 10 shows the contribution of different redshift slices to the total flux function. We contrast this to the flux function using *only* the subsample of 10% radio-loud clusters (black dashed line). This was obtained by constructing the corresponding RLF and repeating the steps above in building an analytical model, however, discarding luminosities $\log_{10} L_{120\,\mathrm{MHz}} \leq 30.75$ in the integration.

In the right panel of Figure 10, we show the total number of RHs that would be *detectable* by the LOFAR Tier 1 survey, where its sky coverage (of about half the entire sky) and the signal degradation due to source extensions of close-by RHs is taken into account. The latter is calculated with Equation (17) and adopting $F = F_{\mathrm{min}}$ where F_{min} is given by Equation (10) of Cassano et al. (2010) as explained above. We clip the flux limit for sufficiently distant RHs at the point-source flux limit $F_{5\sigma}^{\mathrm{PS}}$, i.e., for RHs at $z > 0.6$ we fix $F_{\mathrm{min}} = 0.5$ mJy.

The LOFAR Tier 1 survey at 120 MHz should be able to detect a total of about 3500 clusters hosting RHs above 0.5 mJy. The precise number of detections depends strongly on the underlying assumptions. There are two main uncertainties in our model: the fraction of radio-loud to radio-quiet clusters and the corresponding luminosities as well as our assumed RH modeling in low-mass clusters (which are not yet known to host RHs). The fraction of radio-loud to radio-quiet clusters is determined from a given (degenerate) set of model parameters that include γ_{th}, B_0, α_B, g_{CR}, or equivalently X_{CR}. The fraction of radio-loud clusters mostly affects the number of medium-to-high luminosity RHs (as can be seen from the 1.4 GHz RLFs in the top left panel of Figure 8). The total number of RHs is dominated by low-luminosity RHs. While this may suggest that the radio-loud fraction is of minor importance for the detectable numbers, instead the opposite is the case. Because of the fixed flux limit, only the most luminous clusters at each redshift are observable so that the total number of detectable RHs scales almost linearly with the radio-loud fraction.

We caution that our predicted total number of (detectable) RHs depends on the ability to extrapolate the observed and modeled scalings down to our adopted mass limit of $M_{200} \approx 1.4 \times 10^{14}\, h_{70}^{-1}\, \mathrm{M}_{\odot}$. If the underlying physics imprinted a characteristic scale into the CR transport or magnetic field distribution, this would manifest itself as a break in the radio luminosity scaling relations and dramatically reduce (or even increase) the number of expected RHs. While this does not interfere with previous (high-frequency) measurements at high luminosities, this may of critical importance for future, more sensitive (low-frequency) measurements of low-redshift clusters that probe the uncertain regime of diffuse radio emission in low-mass clusters.

The reason for this lies in the steep halo mass function which ensures that that clusters above a given cutoff (that is either physically motivated or observationally realized through a survey flux limit) dominate the total number of (detectable) RHs. Only if the radio luminosity scaling remains unaltered below the survey flux limit, the steepness of the mass function ensures that there will be more RHs scattered above the flux limit then below it. This is the so-called Eddington bias that causes the inferred luminosities based on only the detected sources to end up as an overestimate. Hence the presence of any hypothetical break in the radio luminosity scaling, which is unconstrained by current data, explains the largely varying model predictions in the recent literature, which vary from a few to hundreds observable RHs (Cassano et al. 2010; Sutter & Ricker 2011) to thousands of detectable RHs in future surveys (Enßlin & Röttgering 2002).

Another relevant issue in such surveys is the identification of RHs and their hosting clusters (see also Cassano et al. 2010). RHs constitute a small part of the entire (diffuse as well as apparent point-like) radio source population and therefore need to be distinguished from the emission produced by other sources. A good approach will be to cross-correlate the radio maps with high-sensitivity X-ray surveys such as that by the future eROSITA mission, which is expected to detect around 10^5 clusters up to redshift $z \approx 1.3$ (see, e.g., Cappelluti et al. 2011).

Our results show the prospects of the LOFAR survey and other future radio instruments in determining the properties over a broad range of RH luminosities. In particular, it should permit a robust determination of the number of clusters hosting RHs at a given luminosity (mass) and to carefully asses completeness issues. This will be extremely helpful in elucidating the RH generation mechanism and in determining the viable parameter space for the hadronic model.

6. Conclusions

We present a detailed model for the population of RHs in galaxy clusters assuming that the radio-emitting electrons are generated through hadronic CR interactions with thermal protons of the ICM. We improve over previous works by phenomenologically exploring the interplay of advective and streaming CR transport in modeling the surface brightness emission, RH scaling relations and luminosity functions. We confirm the theoretical ideas suggested by Enßlin et al. (2011) and explicitly demonstrate that the inclusion of CR streaming is necessary to solve the problems of the *classical* hadronic scenario of radio halos, namely the large extents of giant radio halos in comparison to the thermal X-ray emission and the bimodality of radio-loud and radio-quiet clusters at a fixed X-ray luminosity.

To this end, we use a complete cosmological sample of galaxy clusters selected from the MultiDark N-body simulation (Prada et al. 2012) with redshifts ranging from $z = 0$ to 1. In a next step, we construct a *phenomenological* model for the cluster-gas distribution. This is characterized by X-ray-inferred (CCC and NCCC) gas profiles (taken from the REXCESS sample, Croston et al. 2008) and a cluster-mass-dependent gas fraction (Sun et al. 2009). We assign such a (cluster mass-dependent) gas density profile to each DM halo in our sample and sort it into the NCCC/CCC populations according to a dynamical disturbance parameter that is calculated from the DM distribution. With this model, we obtain a cosmologically complete mock catalog of galaxy clusters that matches the observed $L_{\mathrm{X,bol}}$-to-M_{500}, Y_{X}-to-M_{500}, and Y_{SZ}-to-M_{500} relations, as well as the X-ray luminosity function.

We then construct a new *hybrid* model for the CR distribution in clusters and combine previous results from cosmological simulations and analytical works. We adopt the universal spatial and spectral CR distribution found in hydrodynamic cosmological simulations of cluster formation (Pinzke & Pfrommer 2010), which only account for macroscopic, advective CR transport. Hence, we supplement this model with the approach of Enßlin et al. (2011) that includes the treatment of microscopic CR transport processes. While turbulently-driven CR advection can lead to centrally enhanced CR profiles, CR propagation in the form of CR streaming and diffusion produces flatter CR profiles, which should be realized for decaying cluster turbulence. In our model, we introduce a CR propagation parameter γ_{tu} that is the ratio of the CR streaming-to-advection time scale. This parameter allows us to effectively switch the regimes where either process dominates the CR transport and to explore different turbulent states of the clusters.

This enables us to model the radio surface brightness profiles of giant radio halos (as exemplified in Coma and Abell 2163) as well as of radio mini-halos (in Perseus and Ophiuchus) at 1.4 GHz. We demonstrate that our hybrid CR model can successfully reproduce the radio profiles over the entire extents of giant and mini radio-halos, solving the problems of the *classical* hadronic model. We recover the total radio luminosity within 20% for magnetic field configurations favored by Faraday rotation measurements. Our modeling shows that within the parameter ranges that provide acceptable matches to the radio profiles, the resulting gamma-ray emission from the decay of neutral pions—an inevitable by-product in hadronic CR interactions—is well below observational gamma-ray upper limits provided by *Fermi* and imaging atmospheric Cherenkov telescopes. Future and more sensitive gamma-ray observations, with, e.g., the planned Cherenkov Telescope Array, may in principle be able to disentangle the two competing models for RHs, the hadronic and re-acceleration scenarios.

While we can get excellent matches to the surface brightness of radio mini halos for a range of our CR propagation parameter of $2 \lesssim \gamma_{\mathrm{tu}} \lesssim 100$, in the case of giant radio halos, our model prefers lower values of $1 \lesssim \gamma_{\mathrm{tu}} \lesssim 4$. However, the morphological disturbances in the X-ray and radio maps strongly suggest a highly turbulent state of the ICM in those clusters that host giant radio halos. We discuss that a combination of four effects could artificially lower the inferred values of γ_{tu}: (i) additional radio emission of primary, shock-accelerated electrons in the cluster periphery of these mergers, (ii) an enhanced non-thermal clumping factor in comparison to the thermal clumping factor as suggested by the larger anisotropy of the radio emission (relative to the X-ray emission maps), (iii) a possible spectral steepening in the cluster core region due to CR streaming and diffusive transport that could cause spatial variations of the CR spectral index throughout the cluster and hence a spatially varying radio emission, in particular in the cluster outskirts, and (iv) our choice of simulation-derived CR profiles that may be too concentrated as a result of the overcooling in radiative simulations without AGN feedback.

We select a representative realization of our CR model and compare it with existing radio scaling relations. Because of CR streaming transport and the different gas-density scalings of the X-ray luminosity, $L_{\mathrm{X}} \propto \int \rho_{\mathrm{gas}}^2 \mathrm{d}V$, and the Sunyaev-Zel'dovich flux, $Y \propto \int \rho_{\mathrm{gas}} k_{\mathrm{B}} T \mathrm{d}V$, our model is able to simultaneously reproduce the observed bimodality of radio-loud and radio-quiet clusters at the same L_{X} (Brunetti et al. 2009; Enßlin et al. 2011) as well as the unimodal distribution of radio-halo luminosity versus Y (Basu 2012); thereby suggesting a physical solution to this apparent contradiction. We caution however, that some parameters in our model are degenerate with respect to the resulting radio luminosity and radio emission profiles, in particular γ_{tu} and α_B (our rate of decline of the magnetic field toward the cluster outskirts). Multi-frequency data will be needed to better constrain these parameters and to break these degeneracies.

Assuming a fraction of 10% radio-loud clusters, we demonstrate that our model matches the NVSS radio halo luminosity function (RLF, Giovannini et al. 1999). However, the high-luminosity tail of our model RLF is subject to cosmic variance because of the comparably small simulation volume of $1h^{-3}\,\mathrm{Gpc}^3$. Interestingly, the RLF derived from the $L_{1.4\,\mathrm{GHz}} - L_{\mathrm{X,bol}}$ relation differs at high radio luminosities from the NVSS RLF; possibly because of selection and incompleteness effects that are not fully taken into account. The comparison between different RLFs suggests that the low-luminosity (low-mass) regime is the most promising place to differentiate between various models.

It is expected that the next-generation of low-frequency radio surveys will probe this regime. Hence, we we make prediction for the LOFAR cluster survey, in particular, we compute the 120 MHz RLF and the cumulative RH number density. Given our assumption, we would expect the LOFAR Tier 1 survey at 120 MHz to detect about ~3500 RHs above the flux limit of 0.5 mJy. Since the detectable number of RHs is approximately proportional to the (uncertain) radio-loud fraction, we caution that the precise number depends strongly on the underling assumptions. In particular, we assume that the model parameters can be extrapolated down to cluster masses of about $M_{200} \approx 1.4 \times 10^{14}\ h_{70}^{-1}\ \mathrm{M}_{\odot}$ without any break in the radio scaling relation that would indicate additional scales in the physics. Most of the RHs in our sample lie at low masses and thus at low luminosities that are unconstrained by current observations. If, e.g., the magnetic field and/or the CR distribution in clusters are not statistically self-similar and would exhibit much reduced strength/number density on group scales, our predictions for the detectable number of RHs would be dramatically reduced.

This demonstrates the potential of LOFAR, and other next-generation low-sensitivity radio instruments such as APERTIF, EVLA and SKA, in determining the RLF properties. In combination with future X-ray missions like eROSITA, this should yield a robust determination of the number of clusters hosting RHs at a given luminosity (mass) and thus elucidate the relation of the radio emission with the cluster dynamical state. This will be crucial in determining the parameter values for the hadronic model and eventually in elucidating the RH generation mechanism.

Summarizing, in this work we have constructed a model for the ICM and CR distributions in galaxy clusters that enabled us to provide a cosmologically complete multi-frequency mock catalog for the (non-)thermal cluster emission at different redshifts. We will make these catalogs publicly and freely available on-line through the MultiDark database (www.multidark.org). Those contain the quantities ρ_{gas}, $L_{\mathrm{X,bol}}$, Y_{X}, Y_{SZ}, $L_{120\ \mathrm{GHz}}$, $L_{1.4\ \mathrm{GHz}}$ and L_{γ} (among many others). We hope that the community can make valuable use of these catalogues in synergy with the future radio, X-ray and gamma-ray data.

Acknowledgements. We thank Anders Pinzke for his invaluable help with the formulae and for many useful discussions. We also thanks Gustavo Yepes, José Alberto Rubiño, Frazer Pearce, Andrey Kravtsov, Harald Ebeling, Stefan Gottlöberg, Anatoly Klypin, Miguel-Angel Perez Torres and Adam Mantz for the useful discussions and advices. We thank Matteo Murgia for kindly providing the radio surface brightness profiles of Ophiuchucs and Abell 2163 recomputed with respect to the Reiprich & Böringher (2002) cluster positions, and Wolfgang Reich for providing the radio map of Coma. Finally, we thank the MultiDark database people, in particular Adrian Partl and Kristin Riebe. F.Z. acknowledges the CSIC financial support as a JAE-Predoc grant of the program "Junta para la Ampliación de Estudios" co-financed by the FSE. F.Z. and F.P. thank the support of the Spanish MICINN's Consolider-Ingenio 2010 Programme under grant MultiDark CSD2009-00064. C.P. gratefully acknowledges financial support of the Klaus Tschira Foundation. The MultiDark Database used in this paper and the web application providing online access to it were constructed as part of the activities of the German Astrophysical Virtual Observatory as result of a collaboration between the Leibniz-Institute for Astrophysics Potsdam (AIP) and the Spanish MultiDark Consolider Project CSD2009-00064. The Bolshoi and MultiDark simulations were run on the NASA's Pleiades supercomputer at the NASA Ames Research Center.

References

Abdo, A. A., Ackermann, M., Ajello, M., et al. 2009, ApJ, 699, 31
Abramowitz, M. & Stegun, I. A. 1965, Handbook of mathematical functions with formulas, graphs, and mathematical tables, ed. Abramowitz, M. & Stegun, I. A.
Acciari, V. A., Aliu, E., Arlen, T., et al. 2009, ApJ, 706, L275
Ackermann, M., Ajello, M., Allafort, A., et al. 2010a, ApJ, 717, L71
Ackermann, M., Ajello, M., Allafort, A., et al. 2010b, JCAP, 5, 25
Aharonian, F., Akhperjanian, A. G., Anton, G., et al. 2009a, A&A, 495, 27
Aharonian, F., Akhperjanian, A. G., Anton, G., et al. 2009b, A&A, 502, 437
Aleksić, J., Alvarez, E. A., Antonelli, L. A., et al. 2012, A&A, 541, A99
Aleksić, J., Antonelli, L. A., Antoranz, P., et al. 2010, ApJ, 710, 634
Arlen, T., et al. (for the VERITAS collaboration), Pfrommer, C., & Pinzke, A. 2012, ApJ, accepted
Basu, K. 2012, MNRAS, 421, L112
Battaglia, N., Bond, J. R., Pfrommer, C., & Sievers, J. L. 2011, ArXiv:1109.3709
Battaglia, N., Bond, J. R., Pfrommer, C., Sievers, J. L., & Sijacki, D. 2010, ApJ, 725, 91
Blasi, P. & Colafrancesco, S. 1999, Astroparticle Physics, 12, 169
Blasi, P., Gabici, S., & Brunetti, G. 2007, International Journal of Modern Physics A, 22, 681
Böhringer, H., Collins, C. A., Guzzo, L., et al. 2002, ApJ, 566, 93
Böhringer, H., Tanaka, Y., Mushotzky, R., Ikebe, Y., & Hattori, M. 1998
Bonafede, A., Feretti, L., Murgia, M., et al. 2010, A&A, 513, A30+
Briel, U. G., Henry, J. P., & Boehringer, H. 1992, A&A, 259, L31
Broderick, A. E., Chang, P., & Pfrommer, C. 2012, ApJ, 752, 22
Brown, S. & Rudnick, L. 2011, MNRAS, 412, 2
Brunetti, G. & Blasi, P. 2005, MNRAS, 363, 1173
Brunetti, G., Blasi, P., Cassano, R., & Gabici, S. 2004, MNRAS, 350, 1174
Brunetti, G., Blasi, P., Reimer, O., et al. 2012, ArXiv:1207.3025
Brunetti, G., Cassano, R., Dolag, K., & Setti, G. 2009, A&A, 507, 661
Brunetti, G. & Lazarian, A. 2007, MNRAS, 378, 245
Brunetti, G. & Lazarian, A. 2011, MNRAS, 410, 127
Cappelluti, N., Predehl, P., Böhringer, H., et al. 2011, Memorie della Societa Astronomica Italiana Supplementi, 17, 159
Cassano, R., Brunetti, G., Röttgering, H. J. A., & Brüggen, M. 2010, A&A, 509, A68
Cassano, R., Brunetti, G., Setti, G., Govoni, F., & Dolag, K. 2007, MNRAS, 378, 1565
Cavagnolo, K. W., Donahue, M., Voit, G. M., & Sun, M. 2009, ApJS, 182, 12
Chen, Y., Reiprich, T. H., Böhringer, H., Ikebe, Y., & Zhang, Y.-Y. 2007, A&A, 466, 805
Churazov, E., Forman, W., Jones, C., & Böhringer, H. 2003, ApJ, 590, 225
Croston, J. H., Pratt, G. W., Böhringer, H., et al. 2008, A&A, 487, 431
Deiss, B. M., Reich, W., Lesch, H., & Wielebinski, R. 1997, A&A, 321, 55
Dennison, B. 1980, ApJ, 239, L93
Dolag, K. & Enßlin, T. A. 2000, A&A, 362, 151
Domainko, W., Nedbal, D., Hinton, J. A., & Martineau-Huynh, O. 2009, International Journal of Modern Physics D, 18, 1627
Donnert, J., Dolag, K., Brunetti, G., Cassano, R., & Bonafede, A. 2010a, MNRAS, 401, 47
Donnert, J., Dolag, K., Cassano, R., & Brunetti, G. 2010b, MNRAS, 407, 1565
Dubois, Y. & Teyssier, R. 2008, A&A, 482, L13
Ebeling, H., Edge, A. C., Fabian, A. C., et al. 1997, ApJ, 479, L101+
Eckert, D., Produit, N., Paltani, S., Neronov, A., & Courvoisier, T. J.-L. 2008, A&A, 479, 27
Enßlin, T., Pfrommer, C., Miniati, F., & Subramanian, K. 2011, A&A, 527, A99+
Enßlin, T. A. & Röttgering, H. 2002, A&A, 396, 83
Fabian, A. C., Sanders, J. S., Allen, S. W., et al. 2011, MNRAS, 418, 2154
Fabian, A. C., Sanders, J. S., Taylor, G. B., et al. 2006, MNRAS, 366, 417
Felten, J. E. 1976, ApJ, 207, 700
Feretti, L., Burigana, C., & Enßlin, T. A. 2004, New A Rev., 48, 1137
Feretti, L., Fusco-Femiano, R., Giovannini, G., & Govoni, F. 2001, A&A, 373, 106
Feretti, L., Giovannini, G., Govoni, F., & Murgia, M. 2012, A&A Rev., 20, 54
Ferrari, C., Govoni, F., Schindler, S., Bykov, A. M., & Rephaeli, Y. 2008, Space Science Reviews, 134, 93
Fujita, Y., Hayashida, K., Nagai, M., et al. 2008, PASJ, 60, 1133
Galante, N., Acciari, V. A., Aliu, E., et al. 2009, ArXiv:0907.5000
Giovannini, G., Feretti, L., Venturi, T., Kim, K. T., & Kronberg, P. P. 1993, ApJ, 406, 399
Giovannini, G., Tordi, M., & Feretti, L. 1999, New A, 4, 141
Gitti, M., Brunetti, G., & Setti, G. 2002, A&A, 386, 456
Govoni, F., Murgia, M., Markevitch, M., et al. 2009, A&A, 499, 371
Han, J., Frenk, C. S., Eke, V. R., Gao, L., & White, S. D. M. 2012, ArXiv:1201.1003
Hu, W. & Kravtsov, A. V. 2003, ApJ, 584, 702
Jeltema, T. E. & Profumo, S. 2011, ApJ, 728, 53

Kempner, J. C., Blanton, E. L., Clarke, T. E., et al. 2004, in The Riddle of Cooling Flows in Galaxies and Clusters of galaxies
Keshet, U. 2010, ArXiv:1011.0729
Keshet, U. & Loeb, A. 2010, ApJ, 722, 737
Kiuchi, R., Mori, M., Bicknell, G. V., et al. 2009, ApJ, 704, 240
Klypin, A. & Holtzman, J. 1997, ArXiv:astro-ph/9712217
Kravtsov, A. V., Klypin, A. A., & Khokhlov, A. M. 1997, ApJS, 111, 73
Kravtsov, A. V., Vikhlinin, A., & Nagai, D. 2006, ApJ, 650, 128
Kuchar, P. & Enßlin, T. A. 2011, A&A, 529, A13+
Kushnir, D., Katz, B., & Waxman, E. 2009, J. Cosmology Astropart. Phys., 9, 24
Mantz, A., Allen, S. W., Ebeling, H., Rapetti, D., & Drlica-Wagner, A. 2010a, MNRAS, 406, 1773
Mantz, A., Allen, S. W., Rapetti, D., & Ebeling, H. 2010b, MNRAS, 406, 1759
Million, E. T., Allen, S. W., Werner, N., & Taylor, G. B. 2010, MNRAS, 405, 1624
Miniati, F., Jones, T. W., Kang, H., & Ryu, D. 2001a, ApJ, 562, 233
Miniati, F., Ryu, D., Kang, H., & Jones, T. W. 2001b, ApJ, 559, 59
Murgia, M., Eckert, D., Govoni, F., et al. 2010, A&A, 514, A76
Murgia, M., Govoni, F., Markevitch, M., et al. 2009, A&A, 499, 679
Nevalainen, J., Eckert, D., Kaastra, J., Bonamente, M., & Kettula, K. 2009, A&A, 508, 1161
Pedlar, A., Ghataure, H. S., Davies, R. D., et al. 1990, MNRAS, 246, 477
Pérez-Torres, M. A., Zandanel, F., Guerrero, M. A., et al. 2009, MNRAS, 396, 2237
Perkins, J. S. 2008, in American Institute of Physics Conference Series, Vol. 1085, American Institute of Physics Conference Series, ed. F. A. Aharonian, W. Hofmann, & F. Rieger, 569–572
Perkins, J. S., Badran, H. M., Blaylock, G., et al. 2006, ApJ, 644, 148
Pfrommer, C. 2008, MNRAS, 385, 1242
Pfrommer, C. & Enßlin, T. A. 2003, A&A, 407, L73
Pfrommer, C. & Enßlin, T. A. 2004a, A&A, 413, 17
Pfrommer, C. & Enßlin, T. A. 2004b, MNRAS, 352, 76
Pfrommer, C., Enßlin, T. A., & Springel, V. 2008, MNRAS, 385, 1211
Pfrommer, C., Enßlin, T. A., Springel, V., Jubelgas, M., & Dolag, K. 2007, MNRAS, 378, 385
Pinzke, A. & Pfrommer, C. 2010, MNRAS, 409, 449
Pinzke, A., Pfrommer, C., & Bergström, L. 2011, Phys. Rev. D, 84, 123509
Planck Collaboration, Ade, P. A. R., Aghanim, N., et al. 2011, A&A, 536, A11
Prada, F., Klypin, A. A., Cuesta, A. J., Betancort-Rijo, J. E., & Primack, J. 2012, MNRAS, 423, 3018
Pratt, G. W., Croston, J. H., Arnaud, M., & Böhringer, H. 2009, A&A, 498, 361
Reimer, O., Pohl, M., Sreekumar, P., & Mattox, J. R. 2003, ApJ, 588, 155
Reiprich, T. H. & Böhringer, H. 2002, ApJ, 567, 716
Röttgering, H., Afonso, J., Barthel, P., et al. 2012, Journal of Astrophysics and Astronomy, 34
Sanderson, A. J. R., O'Sullivan, E., & Ponman, T. J. 2009, MNRAS, 395, 764
Sarazin, C. L. 1988, X-ray emission from clusters of galaxies (Cambridge Astrophysics Series, Cambridge: Cambridge University Press, 1988)
Schlickeiser, R. 2002, Cosmic ray astrophysics (Springer. ISBN 3-540-66465-3)
Schlickeiser, R., Sievers, A., & Thiemann, H. 1987, A&A, 182, 21
Sun, M., Voit, G. M., Donahue, M., et al. 2009, ApJ, 693, 1142
Sutter, P. M. & Ricker, P. M. 2011, ArXiv:1110.2786
van Weeren, R. J., Röttgering, H. J. A., Brüggen, M., & Hoeft, M. 2010, Science, 330, 347
van Weeren, R. J., Röttgering, H. J. A., Rafferty, D. A., et al. 2012, A&A, 543, A43
Venturi, T., Giacintucci, S., Brunetti, G., et al. 2007, A&A, 463, 937
Venturi, T., Giacintucci, S., Dallacasa, D., et al. 2008, A&A, 484, 327
Vestrand, W. T. 1982, AJ, 87, 1266
Vikhlinin, A., Markevitch, M., Murray, S. S., et al. 2005, ApJ, 628, 655
Völk, H. J., Aharonian, F. A., & Breitschwerdt, D. 1996, Space Science Reviews, 75, 279
Watanabe, M., Yamashita, K., Furuzawa, A., Kunieda, H., & Tawara, Y. 2001, PASJ, 53, 605
Zimmer, S., Conrad, J., & Pinzke, A. 2012, in American Astronomical Society Meeting Abstracts, Vol. 219, American Astronomical Society Meeting Abstracts, 207.01

Appendix A: Cosmic Ray Modeling Details

Here, we describe in detail how our *hybrid* model for the CR distribution in galaxy clusters of Section 2.5 is constructed by generalizing the analytical results by Enßlin et al. (2011).

As anticipated in Section 2.5, when advection dominates the CR transport, the CR normalization can be expressed as in Equation (10). However, when CR streaming and diffusion dominates, the CR distribution is modified and flattens considerably. This can be shown analytically by solving the continuity equation for CRs and obtaining the CR density profile, $\rho_{\rm CR}$, of Equation (11). Assuming $P(R)/P_0 = n_{\rm e}(R)/n_0$, i.e., neglecting the temperature dependence, and adopting a standard β-profile for the electron density,

$$n_{\rm e} = n_0 \left(1 + \frac{R^2}{R_{\rm c}^2}\right)^{-\frac{3\beta_{\rm cl}}{2}} , \tag{A.1}$$

Enßlin et al. (2011) find that the solution of Equation (11) is physical only for $\rho_{\rm CR}$ within the radial range $R_- < R < R_+$ with

$$R_\pm = \frac{3\beta_{\rm cl}}{2\gamma} R_* \left(1 \pm \sqrt{1 - \left(\frac{2R_{\rm c}\gamma}{3\beta_{\rm cl}R_*}\right)^2}\right) ; \tag{A.2}$$

while it is non-stationary outside these radii. In these regions, the authors suggest to set $\rho_{\rm CR}(R) = \rho_{\rm CR}(R_\pm)$ for $R > R_+$ and $R < R_-$, respectively. Enßlin et al. (2011) obtain the profile for the CR normalization, $C(R) = C_0(\rho_{\rm CR}(R)/\rho_{\rm CR,0})^{\beta_{\rm CR}}$, as

$$C(R) = C_0 \left(1 + \frac{R^2}{R_C^2}\right)^{-\beta_{\rm c}} \exp\left(\frac{R}{R_*}\beta_{\rm CR}\right) \tag{A.3}$$

for $R_- < R < R_+$, where $\beta_{\rm c} = 3\beta_{\rm cl}\,\beta_{\rm CR}/2\gamma$, and $C(R) = C(R_\pm)$ for $R < R_-$ and $R > R_+$, respectively. In this way, different CR transport cases are parametrized through $\gamma_{\rm tu}$. A high value of $\gamma_{\rm tu}$ characterizes the advection-dominated case, while the CR profile is flat for $\gamma_{\rm tu} \sim 1$. We refer the reader to Enßlin et al. (2011) for an extensive discussion.

We want to extend this result to account for (i) our GNFW gas profiles of Section 2.2, (ii) the universal temperature drop in the cluster outskirts, and (iii) merge it with the universal cluster mass-scaling of the CR normalization, $\tilde{C}$, obtained from hydrodynamical simulations (Pinzke & Pfrommer 2010). Therefore, we adopt the hybrid profile, $C_{\rm hybrid} = \tilde{C}(R)(\rho_{\rm gas}(R)/m_{\rm p})(T(R)/T_0)$, of Equation (13). We note that for such a choice, there does not any more exist an analytical solution to Equation (11) as in Enßlin et al. (2011). This results in a 5-order equation and a numerical solution would not be of practical use for every cluster in our large MultiDark sample. For simplicity, we adopt the formulae above also for our hybrid model. I.e., we adopt $C(R) = C_0(\rho_{\rm CR}(R)/\rho_{\rm CR,0})^{\beta_{\rm CR}}$ within $R_\pm$ of Equation (A.2), with $\rho_{\rm CR}$ defined by Equation (11) where $C_{\rm hybrid}$ enters through the advective CR profile, $\eta(R)$, of Equation (12), and $C(R) = C(R_\pm)$ for $R > R_+$ and $R < R_-$, respectively. Note that, in our formalism, $R_{\rm c}$ of Equation (A.2) becomes the characteristic radius of our GNFW gas profile of Section 2.2, i.e., $R_{\rm c} = 0.2R_{500}$, and $\beta_{\rm cl} = 0.8$ (we checked that varying the value of $\beta_{\rm cl}$ between 0.4 and 1.2 has no impact). The relevant factors are $\gamma_{\rm tu}$ and the exponential factor of Equation (11). As we will see in the following, the two radii $R_\pm$ are not critically affected by the form of $\eta(R)$. Therefore, despite the approximation, this approach captures the main CR transport effects.

Assuming our GNFW gas profile instead of a standard β-profile for the electron density, so adopting $P(R)/P_0 = n_{\rm e,GNFW}(R)/n_0$, there exist an exact analytical solution to Equation (11) as in Enßlin et al. (2011). In order to evaluate the systematic error that we are introducing with the approach

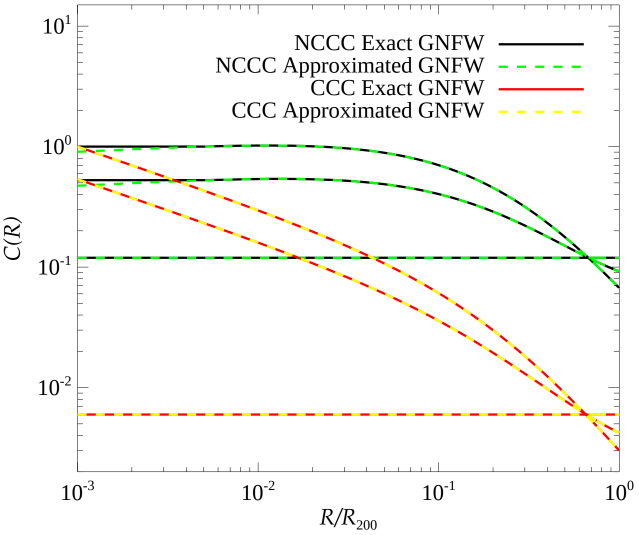

Fig. A.1. Comparison of the exact and approximate solutions for $C(R)$ in the case of our GNFW profile. In the latter case, we use the formulae by Enßlin et al. (2011) but adopt $P(R)/P_0 = n_{\rm e,GNFW}(R)/n_0$ for this comparison only, i.e., we assume here an isothermal ICM. We show the GNFW profiles for NCCCs and CCCs, as derived in Section 2.2. For each of these profile classes, we show three different cases of $\gamma_{\rm tu} = 100$, 10, and 1 (top to bottom). We normalize $C(R)$ for the advection dominated case ($\gamma_{\rm tu} = 100$) at $R = 10^{-3}R_{200}$ and and require CR number conservation during CR streaming. Note that the value for $C(10^{-3}R_{200}, \gamma_{\rm tu} = 100)$ in the CCC case is identical for the exact solution and its approximation, while there is a small difference of about 9% in the NCCC case. We adopt $\alpha = 2.3$.

described above, in Figure A.1, we compare the *exact* solution for $C(R)$ in the case of our GNFW profile with the *approximate* solution where we use the formulae by Enßlin et al. (2011), and only substitute the electron β-profile for our GNFW profiles (with $R_{\rm c} = 0.2R_{500}$, $\beta_{\rm cl} = 0.8$). In this last case, we fix $R_{-} = 10^{-3}R/R_{200}$ to mimic the typical R_{-} value of the exact solution, otherwise an unphysical step feature would appear at $\leq 10^{-2}R/R_{200}$. This latter approximation is kept in our hybrid model, which however has no impact on the model surface brightness and total luminosity. There is almost no difference between the two cases, as shown by Figure A.1. This shows that the approach presented here to construct our hybrid model can be safely followed in order to derive a fully working parametrization which captures the main CR transport effects.

Appendix B: Radio Emission

The factor A_ν in the equation for the radio synchrotron emissivity, Equation (5), is given by (see also Pfrommer et al. 2008 and Enßlin et al. 2011)

$$A_\nu = A_{\rm E_{synch}} \frac{16^{2-\alpha_{\rm e}}\sigma_{\rm pp} m_{\rm e} c^2}{(\alpha_{\rm e}-2)\sigma_{\rm T}\epsilon_{B_{\rm C}} m_{\rm p}} \left(\frac{m_{\rm p}}{m_{\rm e}}\right)^{\alpha_{\rm e}-2} \left(\frac{m_{\rm e}c^2}{\rm GeV}\right)^{\alpha_{\rm e}-1}, \qquad \text{(B.1)}$$

with

$$A_{\rm E_{synch}} = \frac{\sqrt{3\pi}}{32\pi}\frac{B_{\rm c}e^3}{m_{\rm e}c^2}\frac{\alpha_{\rm e}+\frac{7}{3}}{\alpha_{\rm e}+1}\frac{\Gamma\left(\frac{3\alpha_{\rm e}-1}{12}\right)\Gamma\left(\frac{3\alpha_{\rm e}+7}{12}\right)\Gamma\left(\frac{\alpha_{\rm e}+5}{4}\right)}{\Gamma\left(\frac{\alpha_{\rm e}+7}{4}\right)}, \qquad \text{(B.2)}$$

where $\alpha_{\rm e} = \alpha + 1$, the effective inelastic cross-section for proton-proton interactions is $\sigma_{\rm pp} = 32\ (0.96 + {\rm e}^{4.42-2.4\alpha})$, $B_{\rm c} = \sqrt{8\pi\epsilon_{B_{\rm c}}} \simeq 31\,(\nu/{\rm GHz})\ \mu{\rm G}$, and Γ is the Gamma-function (Abramowitz & Stegun 1965). $A_{\rm E_{synch}}$ is given in units of erg, and A_ν is given in units of erg cm^3 g^{-1} sr^{-1}.

The generalization of the radio emissivity, j_ν, to account for three CR populations, each characterized by different power-law spectra and the inclusion of the normalization parameter $g_{\rm CR}$, following Pinzke & Pfrommer (2010), is straight forward. We obtain

$$\begin{aligned} j_{\nu,\rm hybrid} &= g_{\rm CR} C(R) \rho_{\rm gas}(R) \frac{\epsilon_{\rm B}(R)}{\epsilon_{\rm B}(R)+\epsilon_{\rm CMB}} \\ &\times \Sigma_{i=1}^{3} \Delta_i A_{\nu,i} \left(\frac{\epsilon_{\rm B}(R)}{\epsilon_{B_{\rm c}}}\right)^{\frac{\alpha_i-2}{4}}, \end{aligned} \qquad \text{(B.3)}$$

where the sum is over the three CR spectral indexes $\alpha_i = (2.55, 2.3, 2.15)$ with the corresponding factors $\Delta_i = (0.767, 0.143, 0.0975)$ found by Pinzke & Pfrommer (2010).

Appendix C: Gamma-ray Emission

The gamma-ray flux above an energy E_γ is given by (see, e.g., Pinzke & Pfrommer 2010)

$$F_\gamma(>E_\gamma) = \frac{1}{4\pi D^2}\int dV \lambda_\gamma(R)\,, \qquad \text{(C.1)}$$

where the omnidirectional (i.e., integrated over the 4π solid angle) gamma-ray emissivity above E_γ is $\lambda_\gamma(R) = A_\gamma C(R)\rho_{\rm gas}(R)$. The parameter A_γ is (Pinzke & Pfrommer 2010)

$$\begin{aligned} A_\gamma &= g_{\rm CR} D_{\gamma,\rm break} \frac{4 m_{\pi^0} c}{3 m_{\rm p}^2} \Sigma_{i=1}^{3} \Delta_i \frac{\sigma_{{\rm pp},i}}{\alpha_i \delta_i} \left(\frac{m_{\rm p}}{2 m_{\pi^0}}\right)^{\alpha_i} \times \\ &\times \left[\beta_x\left(\frac{\alpha_i+1}{2\delta_i}, \frac{\alpha_i-1}{2\delta_i}\right)\right]_{x_1}^{x_2}, \end{aligned} \qquad \text{(C.2)}$$

where $x_j = \{1 + [m_{\pi^0}c^2/(2E_{\gamma,j})]^{2\sigma_i}\}$, $[\beta_x(a,b)]_{x_1}^{x_2} = \beta_{x_2}(a,b) - \beta_{x_1}(a,b)$ where β denotes the incomplete Beta-function (Abramowitz & Stegun 1965), and $\delta_i = 0.14\alpha_i^{-1.6} + 0.44$. The term $D_{\gamma,\rm break} = D_\gamma(E_\gamma, E_{\gamma,\rm break})$ represents diffusive CR losses due to escaping protons from the cluster at the equivalent photon energy for the break $E_{\gamma,\rm break}$ (see Pinzke & Pfrommer 2010 for details). A_γ is given in units of cm^3 s^{-1} g^{-1}.

Appendix D: Observational Radio-to-X-ray Scaling relation and Luminosity Function

For comparison with the observed 1.4 GHz radio-to-X-ray scaling relation, we include almost all RHs of the sample by Enßlin et al. (2011). We exclude RXCJ1314.4-2515 and Z7160 because they lack bolometric X-ray measurements. We add to our sample the clusters Ophiuchus, A2029 and A1835 (Govoni et al. 2009). The bolometric X-ray luminosities, $L_{\rm X,bol}$, of clusters hosting giant radio halos are taken from Brunetti et al. (2009), while $L_{\rm X,bol}$ values of cluster hosting for mini-halos are taken from Reiprich & Böhringer (2002), Böhringer et al. (1998) and ACCEPT. In the cases where measurement uncertainties for X-ray and radio luminosities are not reported, we adopt a 10% uncertainty. Our final RH sample has a median redshift of $z \approx 0.18$. In the left panel of Figure 7, we show the corresponding radio-to-X-ray scaling relation which is well fit by $\log_{10}(L_{1.4\,\mathrm{GHz}}/h_{70}^{-2}\ \mathrm{erg\ s^{-1}\ Hz^{-1}}) = A + B\ \log_{10}(L_{\mathrm{X,bol}}/h_{70}^{-2}\ \mathrm{erg\ s^{-1}})$, with $A = -37.204 \pm 1.838$, $B = 1.512 \pm 0.041$, and scatter $\sigma_{yx} \approx 0.52$. Regarding the clusters with upper limits on the diffuse radio emission in the sample of Enßlin et al. (2011), we select only those 8 clusters with ACCEPT measurements to obtain a homogeneous data set in $L_{\mathrm{X,bol}}$ (note that there a number of clusters with upper limits on $L_{1.4\ \mathrm{GHz}}$ for which there are only soft-band X-ray luminosities available).

In Figure D.1, we make an attempt to construct an RLF from existing X-ray flux-limited radio surveys. There exist two such studies: the Giovannini et al. (1999) survey with NVSS at 1.4 GHz and the Venturi et al. (2007, 2008) survey with GMRT at 610 MHz by. We only select RHs, i.e., we do not consider radio relics or other diffuse radio emissions of unclear classification. The 1.4 GHz NVSS survey contains 13 RHs out of 205 analyzed clusters while the 610 MHz GMRT survey contains 6 RHs out of the 34 observed. The sample finally analyzed by Venturi et al. (2007, 2008) is composed by 50 clusters and we can also build a corresponding RLF at 1.4 GHz using the 12 present RHs. The fraction of radio-loud clusters is about 6%, 18% and 24% for the NVSS 1.4 GHz, GMRT 610 MHz and GMRT 1.4 GHz sample, respectively. The corresponding median redshift is 0.18, 0.26 and 0.25. We calculate the RLF using the classical V_{max} estimator (see, e.g., Felten 1976) correcting for the sample incompleteness and survey sky coverage. The most problematic aspect in obtaining these RLFs, apart from the few available objects, is the calculation of a meaningful flux limit. We obtain such a limit by fitting the upper envelope of the luminosity-distance distribution of a given sample, as shown in the insets of Figure D.1, following the procedure adopted by Broderick et al. (2012). Note that it is particularly ambiguous to calculate a meaningful flux limit for the GMRT survey due to its poor luminosity-distance distribution. We decide therefore to take the 1.4 GHz NVSS RLF as reference in our comparisons with observation. However, we want to stress that several issues can affect this result, such as the small sample size that impacts the resulting flux limit, and the Malmquist and Eddington biases. Indeed, the very different fraction of radio loud clusters obtained from different samples is one clear indicator of the large uncertainty in the RLF.

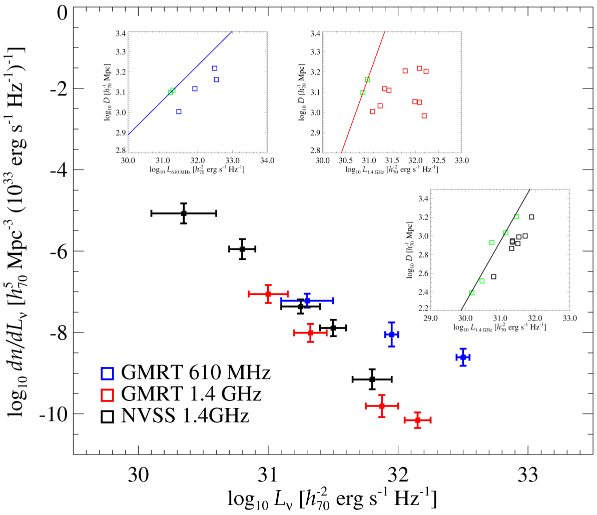

Fig. D.1. RH luminosity function obtained from existent observations. The insets show the sample luminosity-distance distributions (see main text for details) where the solid line is the fit to the upper envelope population (indicated in green) employed to calculate the flux limit for the classical V_{max} estimator. The choice of the upper envelope population is somehow arbitrary, particularly in the GMRT cases due to the poor luminosity–distance distributions. The horizontal error bars represent the mass bins while the vertical error bars are Poissonian uncertainties.